Antimony-bismuth alloying: the key to a major boost in the efficiency of lead-free perovskite-inspired indoor photovoltaics

Basheer Al-Anesi,[1] G. Krishnamurthy Grandhi,[1]* Adriana Pecoraro,[2] Vipinraj Sugathan,[1] N. S. M. Viswanath,[3] Harri Ali-Löytty,[4] Maning Liu,[1] Tero-Petri Ruoko,[5] Kimmo Lahtonen,[6] Debjit Manna,[1] Sami Toikkonen,[1] Ana Belén Muñoz-García,[2] Michele Pavone,[7] Paola Vivo[1]*

[1]*Hybrid Solar Cells, Faculty of Engineering and Natural Sciences, P.O. Box 541, FI-33014 Tampere University, Finland*

E-mail: paola.vivo@tuni.fi; murthy.grandhi@tuni.fi

[2]*Department of Physics "Ettore Pancini" University of Naples Federico II, Comp. Univ. Monte Sant'Angelo 80126 Naples, Italy*

[3]*Division of Materials Science and Engineering, Hanyang University, 222 Wangsimni-ro, Seongdong-gu, Seoul, 04763, Republic of Korea*

[4]*Surface Science Group, Photonics Laboratory, Tampere University, P.O. Box 692, FI-33014 Tampere University, Finland*

[5]*Smart Photonic Materials, Faculty of Engineering and Natural Sciences, Tampere University, P.O. Box 541, FI-33101 Tampere, Finland*

[6]*Faculty of Engineering and Natural Sciences, Tampere University, P.O. Box 692, FI-33014 Tampere, Finland*

[7]*Department of Chemical Sciences, University of Naples Federico II, Comp. Univ. Monte Sant'Angelo 80126, Naples, Italy*

Abstract

Perovskite-inspired Cu_2AgBiI_6 (CABI) absorber has recently gained increased popularity due to its low toxicity, intrinsic air stability, and wide bandgap ≈ 2 eV, which makes it ideal for indoor photovoltaics (IPVs). However, the considerable presence of both intrinsic and surface defects is responsible of the still modest indoor power conversion efficiency (PCE(i)) of CABI-based IPVs, with the short-circuit current density (J_{SC}) being nearly half of the theoretical limit. Herein, we introduce antimony (III) (Sb^{3+}) into the octahedral lattice sites of CABI structure, leading to CABI-Sb with substantially larger crystalline domains than CABI. The alloying of Sb^{3+} with bismuth (III) (Bi^{3+}) induces changes in the local structural symmetry, in turn causing a remarkably increased formation energy of intrinsic defects. This accounts for the overall reduced defect density in CABI-Sb. CABI-Sb IPVs feature an outstanding PCE(i) of nearly 10% (9.53%) at 1000 lux, which represents an almost double PCE(i) compared to that of CABI devices (5.52%) mainly due to an improvement in J_{SC}. This work will promote future compositional design studies to reduce the intrinsic defect tolerance of next-generation wide-bandgap absorbers for high-performance and stable IPVs.

Introduction

The boom of the Internet-of-Things (IoT) urges to address the compelling need of powering an ever-growing number of ubiquitous sensors in a cost-effective, sustainable, and energy-efficient way. Indoor photovoltaics (IPVs) are acknowledged as a key technology to fulfill these requirements, in turn enabling the promised further development of IoT.[1] However, no IPVs have been yet identified that combine high indoor power conversion efficiency (PCE(i)) and reasonable air stability while comprising low-toxicity and abundant constituents. Among the most promising IPV contenders, halide perovskite semiconductors have so far led to the highest PCE(i) thanks to their exceptional defect tolerance, particularly towards intrinsic point defects.[2] Nevertheless, the water solubility and bioaccumulation of lead $(Pb)^{2+}$ cation of halide perovskite compositions pose serious toxicity and recycling concerns. Tin (Sn)-based perovskites, highly investigated for Pb-free solar cells, are not ideal for IPVs due to their narrow bandgap and the known air-instability of Sn^{2+} cation.[3,4] Perovskite-inspired pnictohalides employing cations from Group VA of the periodic table (e.g., antimony (III) (Sb^{3+}) and bismuth (III) (Bi^{3+})) have recently emerged as promising low-toxicity and highly stable absorbers for IPVs, owing to their bandgap of around 2 eV, which is nearly ideal for indoor light-harvesting.[5,6] However, so far only a small handful of IPV studies have been reported[5,7,8,9,10] with PCE(i) values already in the same range of commercially available hydrogenated amorphous silicon (a-Si:H) devices,[11,12] though still far from the maximum theoretical PCE(i) of 50-60%.[5,6] Indeed, all the reported PCE(i) values stagnate around 5–6% at 1000 lux white light-emitting diode (WLED) illumination, with the highest record being so far 6.4%.[10] The reasons for such modest efficiencies lie in the low open-circuit voltage (V_{OC}) and short-circuit current density (J_{SC}) values, mainly due to poor charge carrier transport resulting from abundant intrinsic defects and other typical recombination losses in this class of materials, such as self-trapping.[13,14]

Despite being one of the most recently discovered pnictohalides, Cu_2AgBiI_6 (CABI) has already gained an exceptional interest from the photovoltaic and optoelectronic community owing to its direct bandgap, high absorption coefficient, low exciton binding energy, and the desired band gap of ≈ 2 eV for IPVs.[8,9,15,16,17,18] Several works have contributed to improving CABI discontinuous morphology, consisting of small-sized grains and numerous cracks, by

passivating the surface defects (e.g., via hydroiodic acid additive incorporation,[8] phenethylammonium iodide treatment,[18] or film deposition engineering[17]). Nonetheless, the still suboptimal morphology of CABI films emphasizes the urgent need to enhance grain size and crystallinity. Furthermore, the highly disordered structure of CABI breaks the crystal symmetry, in turn facilitating the formation of intrinsic defects in the bulk. Among them, point defects (e.g., vacancies) are especially important as they largely contribute to irreversible trapping and non-radiative recombination losses.[13] These constrain the performance of photovoltaic devices, particularly in low lighting conditions. Due to the yet ineffective intrinsic and surface defect mitigation, the PCE(i) of CABI-based IPVs is limited to 5.52% at 1000 lux WLED illumination, with the corresponding J_{SC} being 72 μA/cm^2, i.e., nearly half of the theoretical J_{SC} limit predicted for IPVs under the same illuminance.[19] This underlines the need of an extensive defect mitigation strategy to further improve the film morphology and suppress the formation of harmful bulk and surface defects of CABI, in turn bringing the PCE(i) values much closer to the theoretical limit and unlock CABI's full potential in IPVs.

Sb^{3+} co-alloying with Bi^{3+} in pnictohalide absorbers (such as $Ag_2(Bi_{1-x}Sb_x)I_5$, $AgBi_{2-x}Sb_xI_7$,[20] and $CsBi_3I_{10}$)[21] has been proposed as an important approach to enhance the morphology and crystallinity of the films. As a result, the performance of the solar cells based on the Sb-alloyed light harvesters increased, mainly due to the improved J_{SC}. These studies have inspired our strategy of alloying Sb into CABI.

In this work, we fine-tune the incorporation of Sb into the octahedral lattice sites of CABI structure and evaluate the effects on film morphology, structure, charge transport, and device properties. Upon introduction, Sb co-alloys with Bi in CABI and partially replaces it, leading to CABI-Sb. The optimal Bi:Sb molar ratio of 90:10 in CABI-Sb enables a significant improvement in the film morphology, with larger domains having higher crystallinity than CABI. Conversely to other related pnictohalide works, co-alloying of Sb with Bi in CABI (up to the above-mentioned 90:10 Bi:Sb ratio) does not significantly affect neither the nature nor the value of the bandgap. Sb alloying modifies the local structural symmetry of CABI by reducing the lattice distortion and the cation disorder. This leads to a remarkably increased formation energy of intrinsic defects (iodine vacancies), as demonstrated by our theoretical study. As a result, the overall defect density is reduced in CABI-Sb. CABI-Sb photovoltaic devices show a superior performance than CABI counterparts, mainly attributable to an improvement in both J_{SC} and V_{OC}. Our transient absorption (TA) study reveals that, upon the Sb incorporation, a noteworthy suppression of the characteristic self-trapping of the

photoexcited charge carriers in CABI is achieved, which supports the enhanced J_{SC} and overall performance of CABI-Sb devices. CABI-Sb IPVs feature an outstanding PCE(i) of nearly 10% (9.53%) at 1000 lux. This represents a world-record value among all the PIM-based devices and a nearly double PCE(i) compared to that (5.52%) of CABI devices. Our comprehensive device characterization evidences a suppressed trap-assisted and interfacial charge recombination in the CABI-Sb devices due to fewer defects within the domains and/or on the surface of the absorber layer.

This study highlights the great and yet unexplored potential of pnictohalides and promotes future compositional design effort to reduce the defects in the next-generation wide-bandgap absorbers for air-stable IPVs with high efficiency and low toxicity.

Results and Discussion

Structural, optical, and morphological properties of CABI and CABI-Sb

We prepared a series of Sb-alloyed CABI films (referred to as CABI-Sb) by varying the Bi:Sb contents, calculated from the stoichiometric molar ratios of BiI_3 to SbI_3 precursors. The films were deposited through spin-coating and then annealed in air. The detailed fabrication procedure is described in the Experimental section. The structural and optical properties of the various as-prepared CABI-Sb films were examined to identify the most promising CABI-Sb composition for the photovoltaic studies.

CABI crystallizes in a rhombohedral crystal structure with a centrosymmetric $R\bar{3}m$ space group and consists of a single edge-sharing perovskite slab of AgI_6/BiI_6 octahedra (and SbI_6 in the case of CABI-Sb), separated by inorganic Cu^+ cations, referred to as a $CdCl_2$-type rudorffite structure.[15] The structural framework of CABI consists of a highly disordered network in which alternating layers of octahedral sites with the cubic close-packed iodide sublattice are partially occupied by Ag^+ or Bi^{3+} ions (**Figure 1a**). **Figure S1** (Electronic Supplementary Information, ESI) shows the X-ray diffraction (XRD) patterns of CABI-Sb films deposited on glass, with gradually decreasing Bi:Sb ratios of 100:0 (i.e., pristine CABI), 95:05, 90:10, 80:20, 60:40, 40:60, 20:80, and 0:100. The films exhibit nearly identical patterns and crystallize in the rhombohedral crystal structure of CABI in the range of 100:0–40:60 Bi:Sb ratios. However, additional reflections appear near 42°, and the reflection at 13° gradually diminishes, for the samples with Bi:Sb precursor ratios < 90:10. Furthermore, the films with Bi:Sb ratios of 20:80 and 0:100 display XRD patterns dissimilar to those of CABI. Therefore, the samples

predominantly crystallize in the CABI structure only for Bi:Sb ratios higher than or equal to 90:10.

The direct band gap[15] nature of CABI ensures a steep rise in its absorption near the band edge because of the strong excitonic character (**Figure 1b)**. The absorption spectra of CABI-Sb films with Bi:Sb ratios of 95:05 and 90:10 closely resemble that of CABI. Moreover, the band gap of the 90:10 CABI-Sb sample is only negligibly higher by 50 meV compared to that of CABI. On the other hand, decreased band gaps were achieved for Ag-Bi-I and $Cs_2AgBiBr_6$ upon Sb alloying with similar Bi:Sb ratios as in our case.[20,22] It should be noted that in CABI the optical transitions at the band edge involve a dominant contribution of Cu^+ (A-site),[15] which is different than for Ag-Bi-I and $Cs_2AgBiBr_6$. This could explain the negligible influence of Sb on the band gap of CABI. The sharpness of the absorption peak at 590 nm gradually diminishes due to broadening by decreasing the Bi:Sb ratio up to 40:60, and the peak nearly vanishes at the 20:80 ratio. This could be the consequence of the modified band gap nature for the samples with low Bi:Sb precursor ratios. **Figure 1c** shows the variation in the difference between the direct and indirect band gap energies (ΔE) of the films with decreasing Bi:Sb ratios. The small ΔE values of ≈0.03 eV (i.e., 30 meV, which is comparable to the thermal energy of 25.8 meV at room temperature) for the pristine CABI and CABI-Sb samples with 95:05 and 90:10 Bi:Sb ratios indicate a direct band gap nature. The Tauc plots for these samples are shown in **Figure S2**. On the other hand, the increase in the ΔE values (from 0.09 up to 0.28 eV) for the Bi:Sb precursor ratios below 90:10 indicate a gradual direct-to-indirect band gap transition. CABI and CABI-Sb with the lowest Sb content (95:05 and 90:10 Bi:Sb ratios) possess very high absorption coefficient values in the 1.0–2.0 × 10^5 cm^{-1} range near the absorption onset (**Figure S3**), in agreement with the previous study on CABI by Sansom et al.[15] Also, the absorption coefficient values over 10^5 cm^{-1} for CABI and CABI-Sb samples are comparable with those of Ag^+- and Cu^+-based pnictohalides in the 1.6–2.8 eV range.[23,24] The absorption spectrum of CABI on a semi-log scale shows the sub-band gap absorption (**Figure S4**) as in an earlier report.[15] Indeed, the sub-bandgap absorption seems reduced in the CABI-Sb film (Bi:Sb = 90:10), suggesting a lowering of the sub-bandgap state density upon Sb alloying. However, as the scattering effects in the absorption measurements cannot be ignored, such a variation in the sub-band gap absorbance for CABI and CABI-Sb samples will be verified with the analysis of the external quantum efficiency (EQE) spectra of the corresponding photovoltaic devices.[25]

The XRD and absorption studies overall suggest that CABI-Sb samples retain the crystal structure of CABI and exhibit the direct band gap nature only when the Bi:Sb precursor ratio

is ≥ 90:10. Hence, to investigate the hypothesized beneficial effect of Sb co-alloying we focused our characterization on films with a high Bi:Sb precursor stoichiometric ratio. In particular, based on the results of the photovoltaic study performed under 1-Sun illumination (see **Figure S5**), we decided to concentrate on the 90:10 Bi:Sb precursor ratio. Thus, unless otherwise specified, in the following sections we refer to CABI-Sb as the sample comprising a 90:10 Bi:Sb stoichiometric ratio. Both CABI and CABI-Sb films exhibit a great structural stability in the air, as revealed by the nearly unchanged XRD patterns collected over a period of three months (**Figure S6).**

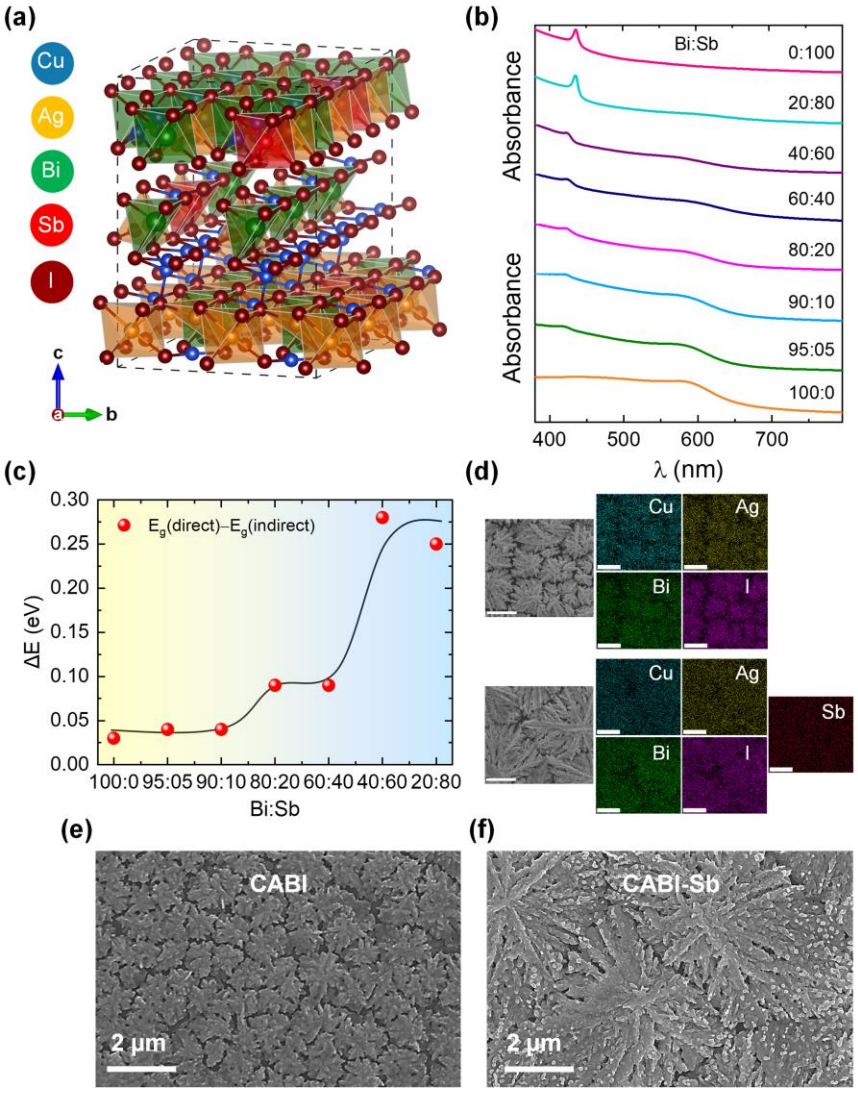

Figure 1. (a) Crystal structure of Sb-alloyed CABI (Bi:Sb = 90:10). (b) Evolution of absorption spectra of CABI-Sb films with decreasing Bi:Sb ratio (from bottom to top). (c) Variation in the difference between the direct and indirect band gap (obtained from Tauc plots) energies with decreasing Bi:Sb ratio. (d) SEM-EDS maps of CABI (top) and CABI-Sb (bottom) films showing the distribution of the elements. Scale bars are 2.5 µm. SEM images of (e) CABI and (f) CABI-Sb films on glass.

The scanning electron microscopy (SEM)-energy-dispersive X-ray spectroscopy (EDS) maps of CABI and CABI-Sb samples (see **Figure 1d**) show a uniform distribution of Cu, Ag, Bi, Sb (for CABI-Sb sample), and I elements with overall compositions of $Cu_2AgBi_{0.71}I_4$ (CABI) and $Cu_{2.4}AgBi_{0.69}Sb_{0.15}I_4$ (CABI-Sb). As earlier,[8,9] the lower (than nominal) bismuth and iodine values is attributed to small quantities of Cu_2BiI_5 and the evaporation of volatile iodine from the surface of the films during the heating process and the strong electron beam exposure.[8,26] The actual Bi:Sb ratio in the CABI-Sb sample according to the EDS analysis is ≈82:18, which is lower than the stoichiometric one (90:10). Our X-ray photoelectron spectroscopy (XPS) study on CABI-Sb also shows a similar Bi:Sb ratio of 82:18 at the surface (see **Table S-XPS)**. The XP survey and core-level spectra of CABI and CABI-Sb films are presented in **Figures S7** and **S8**, respectively. The surface chemical analysis of CABI-Sb and CABI by XPS shows only one component for Cu (Cu $2p_{3/2}$ at 932.8 eV and Cu $2p_{1/2}$ at 952.6 eV), Ag (Ag $3d_{5/2}$ at 368.4 eV), Bi (Bi $4f_{7/2}$ at 159.3 eV), I (I $3d_{5/2}$ at 619.5 eV), and in the case of CABI-Sb for Sb (Sb $3d_{5/2}$ at 531.0 eV and Sb $3d_{3/2}$ at 540.3 eV),which can be assigned to Cu^+, Ag^+, Bi^{3+}, I^-, and Sb^{3+} respectively.[27,28] **Table S-XPS** shows the atomic concentrations at surface (topmost 5–9 nm). Similar to our previous finding on CABI,[8] both the surfaces were partially oxidized (M–O peak at 530.4 eV in O 1s in **Figure S8e**) and show depletion of Cu and enrichment of (Bi and Sb in the case of CABI-Sb) compared to the nominal bulk composition. Most notably, the surface oxidation (M–O) is less pronounced on the surface of CABI-Sb than CABI, suggesting the suppression of iodine vacancy formation by Sb alloying since vacancy formation must precede oxidation. Consequently, the iodine detected on the surface for CABI compared to CABI-Sb is lower (**Table S-XPS).** Our DFT calculations will support and explain the low iodine vacancy formation in CABI-Sb. These findings will be also correlated to the improved photovoltaic performance of the corresponding devices.

The top-view SEM images of CABI and CABI-Sb films (**Figures 1e and 1f**) indicate a clear difference in their domain sizes. While CABI film exhibits crystalline domains smaller than 1 µm in size, the Sb alloying enlarges the domains above 5 µm with an overall significantly increased coverage. Small particles with unidentified nature are observed on the crystalline domains of CABI-Sb (**Figure 1f**), similar to the case of Ag-(Bi:Sb)-I films.[26] The enhanced film morphology of CABI-Sb may arise from the improved solubility of precursors (particularly of AgI and BiI_3) in the presence of Sb^{3+}.[26] Similar improvement in the film morphology was also achieved for Ag-Bi-I films through Sb alloying.[26] Notably, the optimized morphology also translated into enhanced solar cell performance of Ag-(Bi:Sb)-I devices.[26]

Changes in the local structural symmetry

Rietveld refinement was performed on the high-resolution XRD patterns of CABI and CABI-Sb films to determine the phase purity and to investigate any local structural difference between the samples. The refinement results reveal that the XRD patterns of both CABI and CABI-Sb show a full convergence ($\chi^2 < 2$) with the basic model of CABI (**Figures 2a,b**) and no secondary phases are detected in CABI and CABI-Sb films (see **Figure S9** for the refined crystal structures). However, infinitesimal quantities of Cu-B-I impurities may still co-exist.[15] The XRD patterns in **Figures 2a and 2b** also highlight the enhanced grain crystallinity of CABI-Sb sample *vs.* CABI, as evident from the higher intensity of major peak at ≈25° (which corresponds to the (012) plane) in the CABI-Sb pattern. The alloying with Sb retards the crystal growth of the PIM, as we concluded from the slower (nearly 1.5 times) color change (from the initial orange-yellow to the final dark brown) during the annealing steps of CABI-Sb *vs.* CABI films. The prolonged crystallization also explains the film morphology enhancement in the case of CABI-Sb (see **Figures 1e and 1f**) with larger crystalline domains. Our findings are in line with the recent report of Kang et al. dealing with the Sb alloying in $CsBi_3I_{10}$.[21]

The atomic occupancies of Cu^+ (both Cu1 and Cu2), Ag^+, and Bi^{3+} are 0.179, 0.347, and 0.306, respectively (see **Table S1**), which matches well with the previously reported occupancies.[15] The combined occupancy of Bi (0.206) and Sb (0.1) in CABI-Sb equals that of Bi (0.306) alone in CABI (**Tables S1 and S2**), suggesting that the Sb^{3+} ions exclusively occupy some of the octahedral lattice sites of the Bi^{3+} ions in the CABI-Sb structure (see **Figures 1a and 2c**). The refined structure of CABI-Sb also shows an elongated bond length (2.98 Å vs. 2.77 Å) compared to CABI, in agreement with the expansion of the unit cell of CABI in the *c*-direction by 0.1 Å by Sb^{3+} incorporation (see **Table S3**). This finding converses with the typical unit cell contraction observed for Ag-Bi-I and $Cs_2AgBiBr_6$ upon replacing Bi^{3+} with a smaller Sb^{3+} ion.[20,22] We hypothesize that the general rule of size mismatch of the ions may not apply to CABI due to the highly disordered nature of the cations in its crystal structure. For example, the A-site (Cu^+) ions disperse well throughout the structure and dominates the valence band contribution, unlike the cases of Ag-Bi-I and $Cs_2AgBiBr_6$.[15]

The distortion bond angle of Bi-I extracted from the refined structures show a decrease from 103.15º to 101.13º as the result of Sb^{3+} ions alloying in the CABI structure **(Figure 2c)**. Such a significant reduction of the lattice distortion (by ≈2°, which is a large enough value to modify

the optoelectronic properties of metal halide perovskites[29]) implies that the local structural symmetry of CABI-Sb is enhanced over CABI. Furthermore, Sb-alloying at the Bi sites of the crystal lattice of CABI reduces the cation disorder from 0.0077 $(Å)^2$ to 0.0054 $(Å)^2$. In lead halide perovskites (LHPs), a reduced octahedral distortion has led to the suppression of the pathways by which ions migrate and defects trap the photogenerated charge carriers with a consequent improvement of the corresponding solar cells performance and stability.[30,31] Chen et al. reported that changes in the local lattice distortion at a low temperature eliminates the intrinsic defects by increasing the formation energy of the iodine vacancies and the interstitial defects in triple-cation LHP solar cells.[31] Saidaminov et al. also demonstrated that lattice strain relaxation by small cation incorporation at the B-site suppresses the iodine vacancy formation in LHPs.[32] Further, an improvement in the charge carrier collection of LHP and Sn-perovskite devices attributed to a reduced lattice distortion was reported by Nishimura et al. and Zhu et al.[33,34] All these studies suggest that the local structural symmetry enhancement upon Sb introduction in the CABI structure could lead to performance enhancement in the corresponding photovoltaic devices, as will be demonstrated in the following sections.

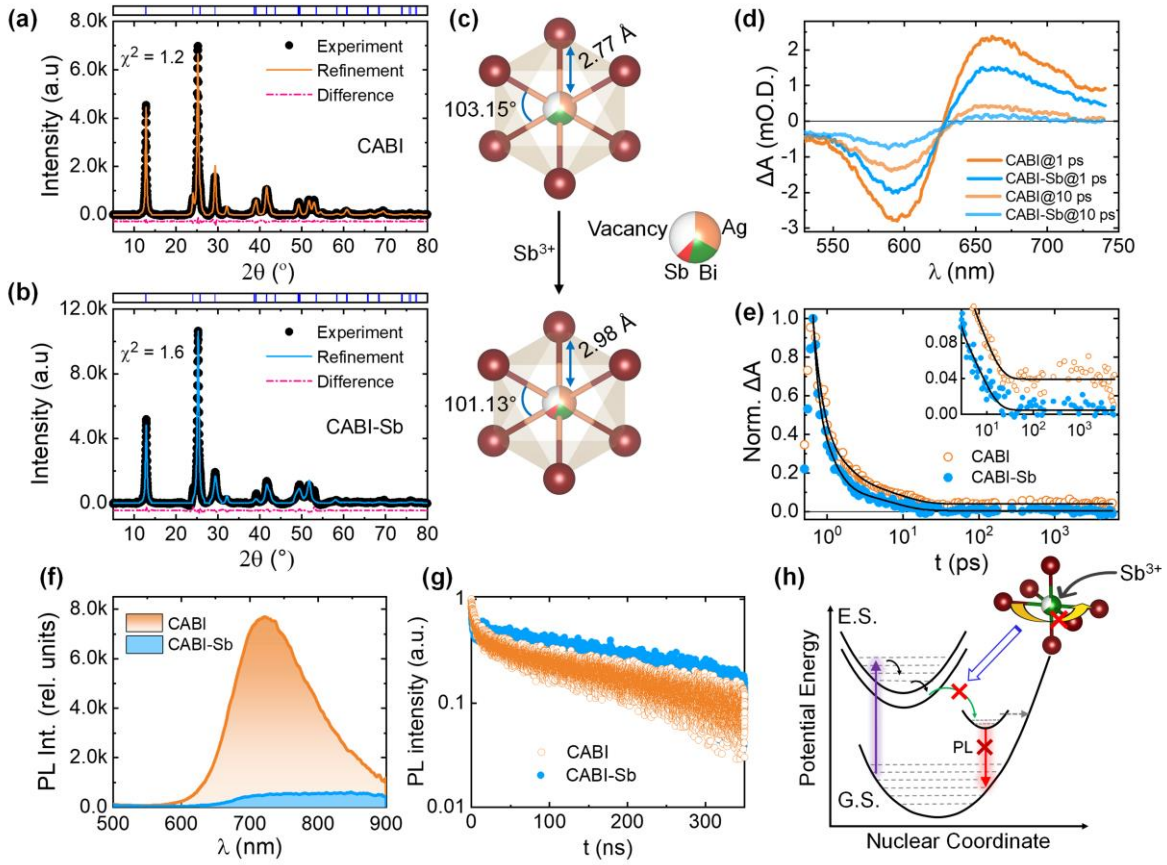

Figure 2. Experiment (closed circles), refinement (solid line), and difference (dashed line) profiles obtained after full-pattern Rietveld refinement of (a) CABI and (b) CABI-Sb. (c) shows

the average bond length and distortion angle of BiI_6 before and after the alloying of Sb^{3+} ions into the lattice. (d) Ultrafast transient absorption (TA) spectra of pure CABI and CABI-Sb films, excited at 400 nm with an excitation energy density of 20 μJ cm^{-2}. (e) TA decays for pure CABI and CABI-Sb films, monitored at 660 nm. Solid lines represent the fits corresponding to a tri-exponential function: $\Delta O.D. = A_1 \exp\left(-\frac{t}{\tau_1}\right) + A_2 \exp\left(-\frac{t}{\tau_2}\right) + A_3 \exp\left(-\frac{t}{\tau_3}\right)$ for pure CABI film and with a bi-exponential function: $\Delta O.D. = A_1 \exp\left(-\frac{t}{\tau_1}\right) + A_2 \exp\left(-\frac{t}{\tau_2}\right)$ for CABI-Sb film, respectively. $\Delta O.D.$ is the change in optical density. (f) PL spectra and (g) TRPL decay curves of CABI and CABI-Sb films on glass. (h) Schematic of the adiabatic potential energy curves of the ground state (G.S.), excited state (E.S.), and a low-energy excited state (i.e., STE state) along with the horizontal dashed arrow indicating the possible non-radiative process in a configuration space, under 400 nm photoexcitation. Sb^{3+}-mediated suppressed excited-state octahedral distortion, thereby reducing carrier self-trapping, is also depicted.

Suppressed carrier self-trapping in CABI through Sb alloying

CABI is known to exhibit a weak self-trapped exciton (STE) emission by excited-state octahedral distortion,[16] with the origin of the emission yet to be understood.[8] It is, thus, reasonable to believe that the above-discussed improvement in the local structural symmetry of CABI-Sb may have serious implications on its STE properties.[35,36] To investigate the influence of Sb alloying on the charge carrier dynamics of CABI in excited state, we conducted ultrafast TA measurements on CABI and CABI-Sb films. **Figure 2d** shows the comparison between the TA spectra of the two films, which were excited at 400 nm and monitored at pump-probe time delays of 1 ps and 10 ps. The TA spectra demonstrate a strong photo-bleaching (PB) characteristic (negative ΔO.D.) and a broad photo-induced absorption (PIA) band (positive ΔO.D.) centered at around 595 nm (~2.08 eV) and 660 nm (~1.88 eV), respectively, in both the cases. It is noteworthy that the PB peak positions do not match with their steady-state absorption onsets, which rather possess an almost identical position as their first exciton peaks (see **Figure 1b**). This suggests that the absorption onsets of both films consist of an exciton absorption band and an absorption continuum, which are not spectrally resolved.[23] The broad and asymmetric PIA bands at longer wavelengths confirm the formation of STEs. Interestingly, the amplitude of the PIA bands in pure CABI compound at the same time delay (e.g., one ps or ten ps) is decreased upon Sb alloying at the Bi lattice sites. This indicates that the involvement of Sb in the CABI structure can effectively reduce the number of self-trapped excitons, in agreement with the enhanced symmetry at the octahedral sites of the structure highlighted by our XRD analysis.[35] The charge transfer dynamics were studied by recording the TA decays at 660 nm (**Figure 2e**). The decays of CABI and CABI-Sb samples were well

fitted with a tri-exponential and a bi-exponential function, respectively (see the fitting results in **Table S4**). The ultrafast (t_1 <1 ps) and fast (t_2 of ~4 ps) components of the two decays can be assigned to the localization of free charge carriers, i.e., self-trapping of the excitons, and non-radiative transitions, respectively.[16,8] In the case of CABI, we assign the slow decay component (t_3 of > 4 ns) to the radiative recombination of STEs.[35,37] On the other hand, the contribution of the slow (radiative) component to the TA decay of CABI-Sb film is negligible, further suggesting the suppressed STE recombination through Sb incorporation. Subsequently, the photoluminescence (PL) intensity of CABI film is quenched through alloying with Sb (**Figure 2f**). The corresponding TRPL (time-resolved PL) decay curves (**Figure 2g**), collected at their emission maxima, show comparable decay behavior and radiative lifetime values (484 ns and 356 ns for CABI and CABI-Sb films, respectively, as given in **Table S4**). This suggests that the emission quenching observed in the CABI-Sb sample can be attributed to the reduced carrier self-trapping rather than a lower STE recombination efficiency compared to CABI. We, thus, conclude that the population of generated STEs is significantly reduced upon introducing Sb into the octahedral lattice sites of the CABI structure (see **Figure 2h**). It is interesting to compare that the alloying of Sb into $Cs_2AgBiBr_6$ quenched its PL intensity;[38] however, in that case, the quenching is associated with the loss of more excitons in stark contrast to the case of CABI-Sb. The reduced carrier mobility associated with self-trapping in CABI[16] leads to low drift and diffusion lengths.[14] The suppressed self-trapping of the photoexcited carriers in the case of CABI-Sb results in a higher number of free excitons than in pristine CABI, leading to more effective charge separation and extraction, which, in turn, may enable an enhanced J_{SC} and device performance in CABI-Sb photovoltaics.[14]

Electronic band structures and defect formation energy from first-principles calculations

We performed a theoretical investigation of the structural and electronic features of CABI and CABI-Sb via state-of-the-art density-functional theory (DFT) calculations. Starting from the parent CABI structure with Cu_2AgBiI_6 composition, we built a model for CABI-Sb by partially replacing bismuth atoms with antimony such that the Bi:Sb ratio was 13:3 (= 78:18), i.e., closely matching the Bi:Sb ratio in CABI-Sb experimentally determined by EDS and XPS. While the computational details are provided in the Experimental section, the structural models for the calculations are presented in the ESI. Relaxed structures for both compounds are shown in **Figure S10**. The evaluated lattice constants and band gap values are collected in **Table S5**. Incorporation of Sb does not significantly alter the CABI structure; only slight contractions of the lattice constants are observed in *a* and *b* directions ($\approx 0.34\%$ and $\approx 0.13\%$, respectively)

while the most significative change is a 1.3% elongation in the *c* direction, which confirms the experimentally observed trend (see **Table S3**).

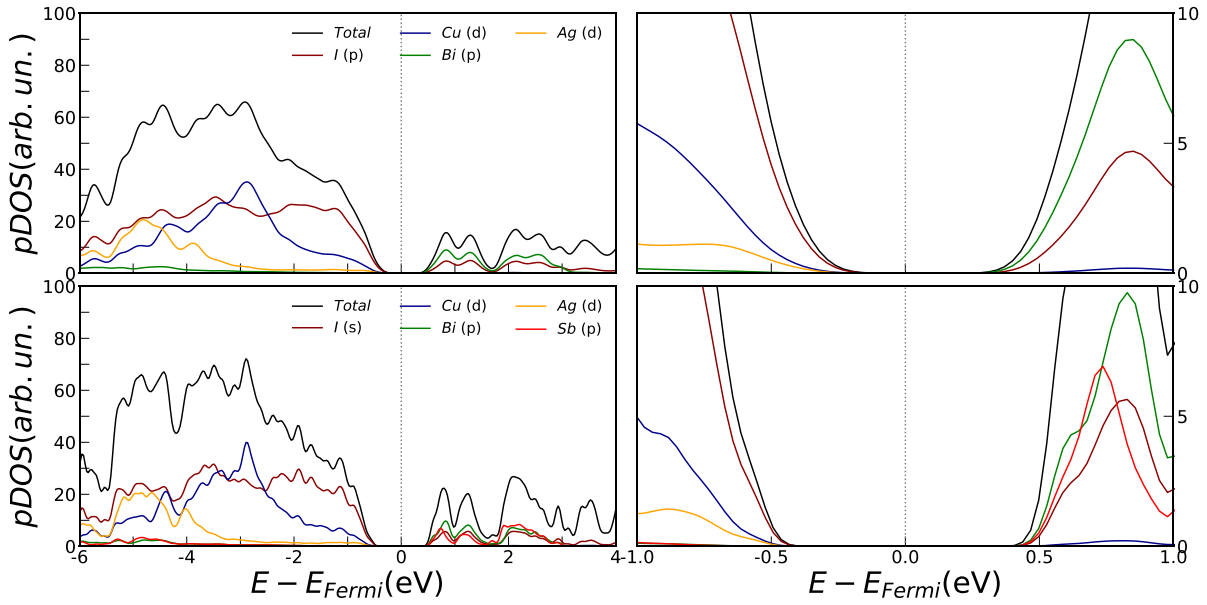

Figure 3. Spin-averaged, atom- and angular-momentum projected density of states (pDOS), calculated at the spin-polarize HSE06+TS level of theory for: CABI and its magnification around the Fermi level; upper left and upper right panels, respectively. pDOS of CABI-Sb and its magnification around the Fermi level; lower left and lower right panels, respectively. Color legend: Total, black; Cu, blue; Ag, orange; I, purple; Bi, green; Sb, red.

Electronic features have been analyzed through evaluation of the projected density of states (pDOS) shown in **Figure 3.** The main contribution to the valence band (VB) of CABI comes from copper and iodine, while the conduction band (CB) is dominated by bismuth and iodine p states, in agreement with previous works.[15] VB composition is insensitive to the Sb alloying, while a contribution of antimony *p* states arises in the CB of CABI-Sb. The band gap values reported in **Table S5** for both CABI and CABI-Sb are 0.99 eV and 1.10 eV, respectively, and have a direct nature, supporting the Tauc plot analysis (**Figure S2**). Despite the expected poor quantitative agreement with experimental band gap values, our first-principles calculations correctly demonstrate the nature of electronic transition and can qualitatively reproduce the experimental observed trend.

We investigated the effect of intrinsic iodine defects on the electronic structure of both CABI and CABI-Sb. A point defect was mimicked by eliminating one neutral iodine atom from the

structures of both CABI and CABI-Sb. We considered different positions for the vacancy with different local chemical environments. For CABI, we considered two separate cases, namely the removal of an iodine atom both from a BiI_6 and a AgI_6 octahedra. The SbI_6 case was additionally considered for CABI-Sb. These defects are denoted as $V_{I(Ag)}$, $V_{I(Bi)}$ and $V_{I(Sb)}$, respectively. Formation energy for each defect was calculated as:

$$E_{form} = E_{def} + \frac{1}{2}E_{I_2}^{(g)} - E_{pristine}$$

where E_{def} , $E_{I_2}^{(g)}$and $E_{pristine}$ are the total energies of the defective structure of an isolated iodine molecule (in gas phase) and of the pristine structure, respectively. **Table 1** shows the as-calculated formation energy values. Higher formation energies obtained for CABI-Sb than CABI suggest that Sb-alloying inhibits the defect formation process and increases the value up to about 1 eV in the $V_{I(Ag)}$ case. The corresponding impact on the electronic features has been investigated through pDOS, as reported in **Figure 4.**

Table 1. Vacancy formation energy for iodine defects with different local chemical environment, calculated at HSE06+TS level of theory.

	Formation energy (eV)		
	$V_{I(Ag)}$	$V_{I(Bi)}$	$V_{I(Sb)}$
CABI	0.39	1.64	-
CABI-Sb	1.37	2.26	2.16

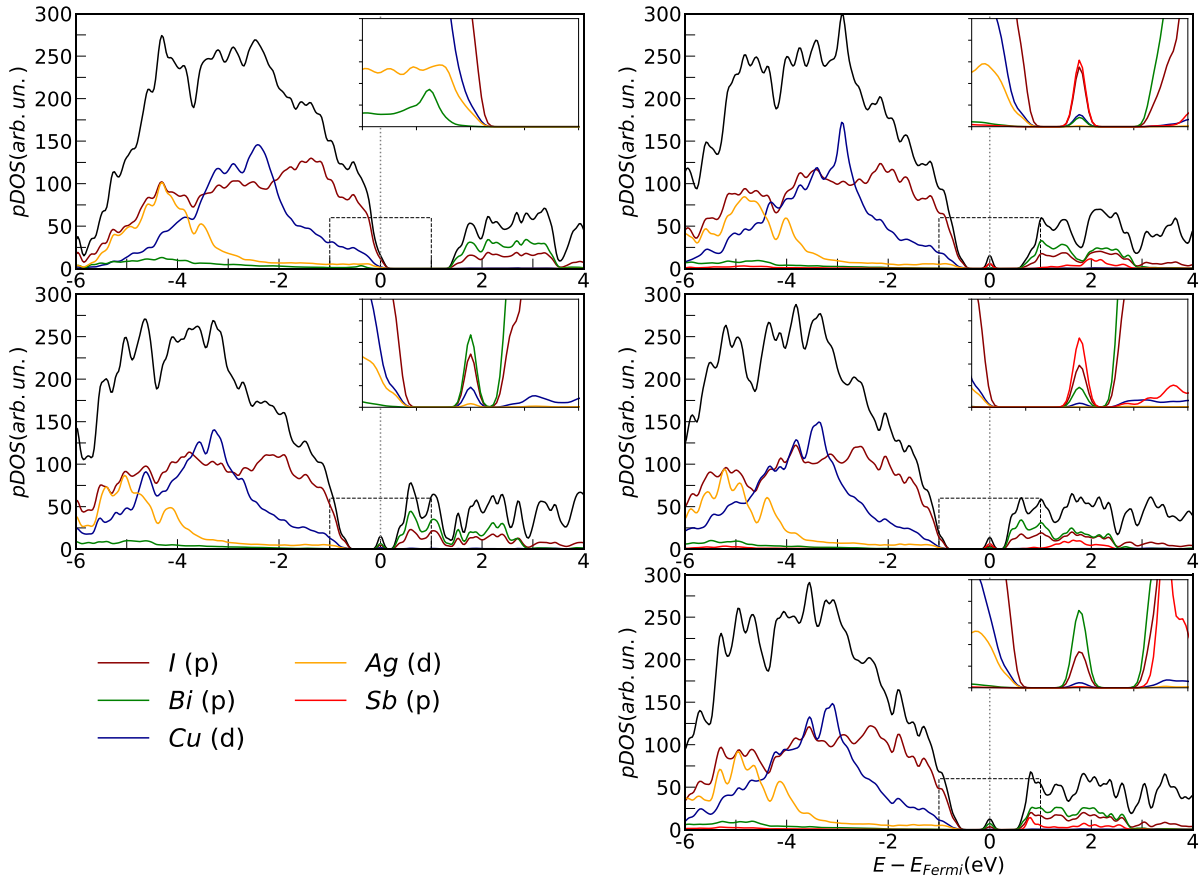

Figure 4. pDOS for CABI (left column) and CABI-Sb (right column) pertaining to three defect location cases: $V_{I(Ag)}$, first row; $V_{I(Bi)}$, second row; $V_{I(Sb)}$, third row. Color legend as in Figure 3**.** Insets in upper right part of each plot are a magnification of the surrounding of the Fermi level highlighted by the dotted squared frame.

The introduction of a defect does not modify the composition of frontier bands in any of the two cases. Different responses to $V_{I(Ag)}$ defect occur for the two compounds. In the case of CABI, a Fermi level crossing occurs for the VB, suggesting a slight p-type doping, while in CABI-Sb the defect produces a mid-gap state in correspondence with the Fermi level. Similar defect states occur in all the other cases. The main contribution to these states comes from Sb p states for the $V_{I(Ag)}$ and $V_{I(Bi)}$ in the CABI-Sb, while being dominated by Bi p states both for CABI $V_{I(Bi)}$ and CABI-Sb $V_{I(Sb)}$.

Overall, DFT results highlight that, for the considered CABI-Sb composition, alloying with Sb at the Bi lattice sites does not significantly alter neither the structure nor the electronic properties of CABI. On the other hand, the Sb alloying has a beneficial effect since it significantly increases the iodine vacancy formation energies, thus, preventing unintentional doping or mid-gap trap states from arising. The reduced intrinsic defect density in CABI-Sb is

advantageous for improved charge collection from the corresponding photovoltaic devices, particularly at low-light intensity illuminations, where the charge carrier generation is small. The experimental validation of the reduced defect density in CABI-Sb compared to CABI is achieved through space-charge limited current (SCLC) measurements (see the Trap density section), and its consequences on the photovoltaic device performance under 1-Sun and indoor illuminations are demonstrated in the following sections.

Solar cell performance

To verify our hypothesis that the Bi:Sb co-alloying is essential to improve the performance of corresponding photovoltaics, we fabricated complete device stacks with an *n-i-p* mesoscopic structure featuring CABI or CABI-Sb as the light absorber. Complete details on the fabrication are provided in the Experimental section. The mesoscopic architecture was chosen since it is known to result in higher efficiencies than the planar counterpart for CABI-based devices.[9,17] The full device configuration, i.e., FTO|c-TiO_2|mp-TiO_2|absorber (CABI or CABI-Sb)|Spiro-OMeTAD|Au, relied on standard electron- (ETL) and hole-transport (HTL) layers, namely compact (c-) and mesoporous (mp-) TiO_2 ETL and 2,2',7,7'-Tetrakis[N,N-di(4-methoxyphenyl)amino]-9,9'-spirobifluorene (Spiro-OMeTAD) HTL (see **Figure 5a**). **Figure S11** displays the cross-sectional view of a representative CABI-Sb device. A thickness of 200–250 nm for the mp-TiO_2 layer was targeted to maximize the CABI device performance according to an earlier study.[9] The photoactive layers' thickness of ~300 nm enables the absorption of most of the incident light due to the high absorption coefficients of CABI and CABI-Sb (see **Figure S3**).

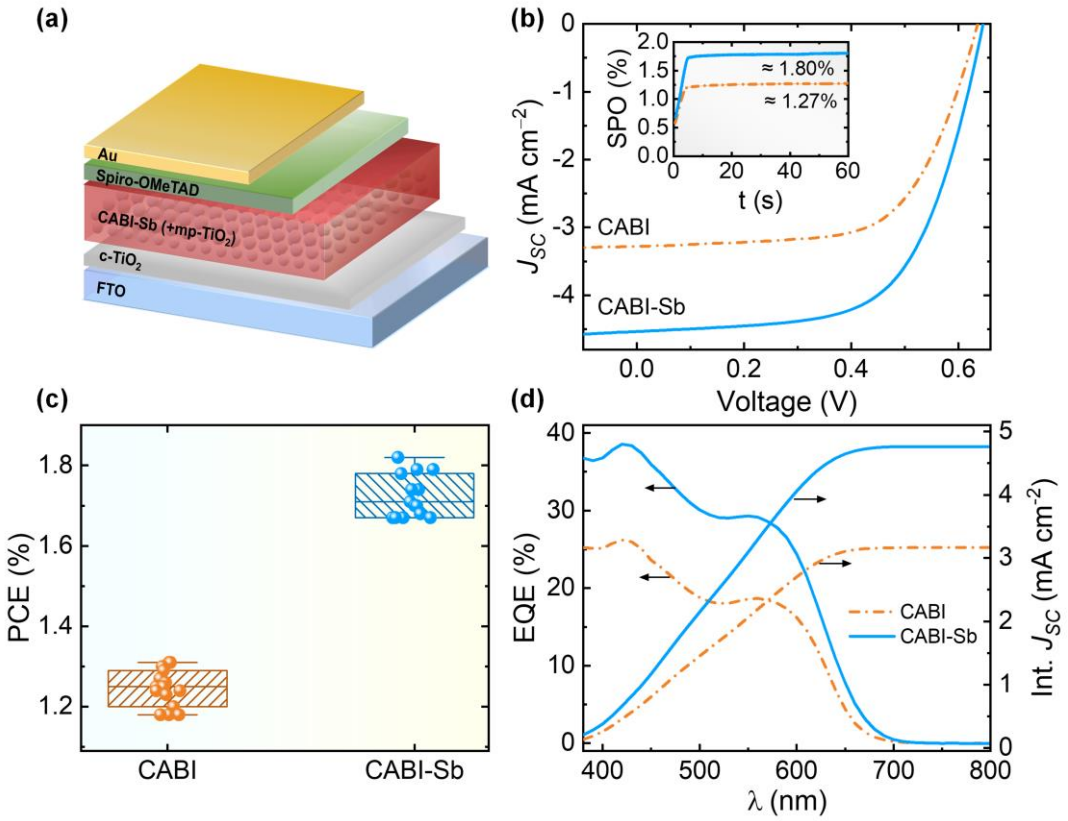

Figure 5. a) Scheme of a typical device stack for CABI-Sb photovoltaic cell. b) *J*–*V* curves (reverse bias scans) of the best CABI and CABI-Sb devices under 1-Sun illumination. The inset shows the stable power output (SPO) behavior of the devices near the MPP under continuous 1-Sun illumination intensity. c) Statistical distribution (over 15 devices) of the photovoltaic parameters of CABI and CABI-Sb devices (device active area 0.20 cm^2) under 1-Sun illumination. d) EQE spectra and the integrated J_{SC}^{EQE} curves of the devices.

The performance of the photovoltaic devices was first evaluated under 1-Sun illumination (AM 1.5 G, 100 mW cm^{-2}). **Figure 5b** shows the comparison between the current density (*J*)–voltage (*V*) curves of the champion CABI and CABI-Sb devices. We verified the reliability of the PCE of the devices by conducting stable power output (SPO) measurements under maximum power point (MPP),[39] as shown in the inset of **Figure 5b**. The statistical distribution of PCE values of the devices is presented in **Figure 5c**, and the box charts of fill factor (FF), J_{SC}, V_{OC} can be found in **Figure S12**. While the champion CABI device displays a PCE of 1.31% (consistently with our previous report),[9] the PCE of 1.82% of the best-performing CABI-Sb device is the highest value ever reported for CABI-based planar and mesoscopic solar cells with Au metal electrode.[15,8,17,9,18] The SPO values of the CABI (≈1.27%) and CABI-Sb (≈1.80%) in the inset of **Figure 5b** closely match their PCE values of 1.31% (CABI) and 1.82% (CABI-Sb). The

average PCE of CABI-Sb devices is 1.72% and the PCE trend (**Figure 5c**) confirms that in each case they outperform the cells employing a pristine CABI absorber (average PCE =1.25%). The improvement in the V_{OC} values of CABI-Sb devices by 35 meV compared to pristine CABI cells suggests the decrease in the number of traps that act as recombination centers upon Sb co-alloying. The boosted J_{SC} (by 1.46 times) is evidently the major contributor to the enhanced PCE of CABI-Sb devices (see **Table 2**). In earlier works on Ag-Bi-I absorbers, the B-site (Bi) co-alloying with Sb led to morphology enhancement of the films (particularly in terms of increased grain size) and blue-shifted bandgap.[20,40] As a result, the PCE of the cells employing Sb-alloyed absorbers was enhanced due to increased photocurrent. In this work, the improved microstructure of CABI films upon Sb alloying is also demonstrated (see **Figures 1e and 1f**) but we believe this being only partially responsible of the J_{SC} increase. Furthermore, the addition of Sb in our case has an insignificant effect on the bandgap tuning up to 50 meV, and CABI and CABI-Sb layers have comparable thickness (and, thus, absorption). The important role of Sb alloying in reducing the defect tolerance of CABI absorber (as shown in the previous section on the first-principles calculations) leads to a lowered defect density (quantitatively demonstrated by SCLC-based measurements in the Trap density section). This, in turn, relates to a more effective charge collection in CABI-Sb *vs*. CABI, which we can directly connect to the increase in J_{SC}. The enhanced J_{SC} in CABI-Sb devices is in line with the anticipated enhanced exciton generation owing to the suppressed carrier self-trapping in CABI through Sb alloying.

Table 2. Average (15 devices) photovoltaic parameter values of CABI and CABI-Sb devices under 1-Sun illumination.

	PCE (%)	FF (%)	J_{sc} (mA/cm^2)	V_{oc} (V)
CABI	1.25±0.05	65.5±0.87	3.12±0.13	0.64±0.01
CABI-Sb	1.72±0.05	66.2±0.60	4.56±0.04	0.675±0.016

The shelf-life stability of unencapsulated CABI and CABI-Sb devices (stored in dry air with 20% RH at 25 °C) was monitored (see **Figure S13**). During the initial 40 days, the CABI-Sb devices shows no PCE drop, and they still retain 82% of the initial PCE after 100 days of storage. On the other hand, the initial PCE of the pristine CABI device decreases to 80% already after 20 days, and it remains at only 46% of the initial value after 80 days. The PCE loss in both devices is mostly mediated by the gradual decrease in their J_{SC}. However, the much

slower fall of J_{SC} in the CABI-Sb device than in the CABI one indicates a slow degradation of CABI-Sb absorber layer, which guarantees an enhanced stability of the corresponding devices. The improved FF in the first 50 days of air storage of CABI-Sb device originates from the gradual increase in the conductivity of doped Spiro-OMeTAD,[41] which compensates the initial J_{SC} loss, in turn assuring a nearly unchanged PCE in the first 40 days. On the other hand, the lack of FF improvement in the pristine CABI device may be due to the extremely fast degradation of CABI absorber layer, which does not allow benefiting of the effect of Spiro-OMeTAD on the FF.

The integrated J_{SC} values of the two devices from their external quantum efficiency (EQE) spectra match well (within a minor deviation <5%) the J_{SC} values obtained from the *J–V* measurements (**Figure 5d**). CABI-Sb devices show higher EQE than the CABI reference in the 350–700 nm range (**Figure 5d**). This supports the above-mentioned higher charge collection efficiency in CABI-Sb absorber, which is reflected in the improved J_{SC} of the corresponding devices (see **Figure S12** and **Table 2**). By analyzing the region where the EQE decreases exponentially with decreasing energy (i.e., the sub-band gap region), we can also obtain insights into the density of sub-band gap state distribution (i.e., localized exponential-tail states)[15]. The Urbach energy (E_U)[25,42] can be estimated from the following correlation:

$$\text{EQE} \propto \text{absorption coefficient} \propto e^{\frac{E-E_g}{E_U}}$$

The extracted E_U values for CABI and CABI-Sb devices are 49.6 meV and 47.6 meV, respectively (**Figure S14**). These are higher than the typical values for LHPs (e.g., 13.5 meV for triple cation-based device)[42] but lower than those of Sb-alloyed $Cs_2AgBiBr_6$ (~90 meV).[38] The reduced E_U value in the case of CABI-Sb devices indicates a lower energetic distribution of sub-band gap trap states, which may be ascribed to the enhanced symmetry and reduced cation disorder of CABI-Sb structure over CABI evidenced from the structural refinement study (see **Figures 2a−2c** and the related discussion). Such a favorable trap energy distribution may mitigate undesirable carrier recombination through the trap states in CABI-Sb, in turn leading to superior performance of CABI-Sb devices.[25,43]

The higher internal quantum efficiency (IQE) (**Figure S15**) of the CABI-Sb cell with respect to CABI reference suggests that a larger portion of the absorbed photons are converted into free carriers, as confirmed by the reduced self-trapping demonstrated by the TA and PL characterization. The free carriers are then successfully collected at the corresponding electrodes in agreement with the superior EQE response of CABI-Sb devices.

The enhancement in the J_{SC} of the CABI-Sb devices could also be associated with a high shunt resistance (R_{Sh}). The champion CABI-Sb device displays a R_{Sh} of 5.1×10^4 Ω cm^2 (extracted from dark *J*–*V* curve), which represents a noticeable increase in comparison with that of the pristine CABI devices in this work ($R_{Sh} = 1.8 \times 10^4$ Ω cm^2) and from our previous study.[8] The enlarged domains in the CABI-Sb absorber layer (**Figure 1f**) reduce the number of pin holes or the shunt pathways, in turn ensuring diminished leakage of the photogenerated current of the corresponding photovoltaic device.

Indoor photovoltaics

The variation in the R_{Sh} between CABI and CABI-Sb devices strongly influences their performance under low-intensity indoor illumination (<10 mW cm^{-2}), which produces a limited number of photogenerated charge carriers.[44,45] Furthermore, the good match between the EQE spectrum of CABI-based devices and the emission spectrum of a WLED suggests that higher PCE can be achieved under WLED illumination than 1-Sun (**Figure 6a**).[8,9] While the champion CABI device delivers a PCE(i) of 5.52% (in line with what was reported earlier),[9] the highest PCE(i) of 9.53% (see **Figure 6b** for the corresponding *J*–*V* curves) is achieved under 1000 lux (**Figure 6c**). The average PCE(i) values were 5.26% and 8.29% for CABI and CABI-Sb devices, respectively. The 1.6 times increase in the average PCE(i) upon Sb co-alloying is majorly due to the enhancement in the J_{SC} values (see **Table S6** and **Figure 6c**), as in the above-discussed case of 1-Sun illumination. The incorporation of Sb into CABI devices leads to improvement of the J_{SC} from 72 μA cm^{-2} to 127 μA cm^{-2} at 1000 lux, which is now much closer to the theoretical limit at the same illuminance (≈143 μA cm^{-2}).[19] Slight improvements in FF and V_{OC} are also observed for the CABI-Sb IPV devices. The PCE(i) of 9.53% for the best CABI-Sb device is the highest value ever reported for IPVs based on lead-free perovskite-inspired absorbers (with the previous record being 6.37% for CsMAFA-Sb pnictohalide[10]). This value also represents a remarkable advancement of the performance of CABI-based IPVs, bringing it a step closer to the theoretical PCE(i) limit (50–60%)[5,8] and confirming the enormous potential of this family of semiconductors for low-toxicity IPVs stemming from inexpensive and easily available materials. It is interesting to note that, despite a moderate PCE (1.82%) under 1-Sun illumination, for instance, compared to the recently reported CsMAFA-Sb (2.47%),[10] CABI-Sb devices deliver higher PCE(i) under 1000 lux WLED illumination than the Sb-based (CsMAFA-Sb) pnictohalide photovoltaics. This is majorly due to a greater match between the excitonic absorption feature of CABI-Sb and the emission spectrum of WLED in the 500–700 nm range (**Figure 6a**).

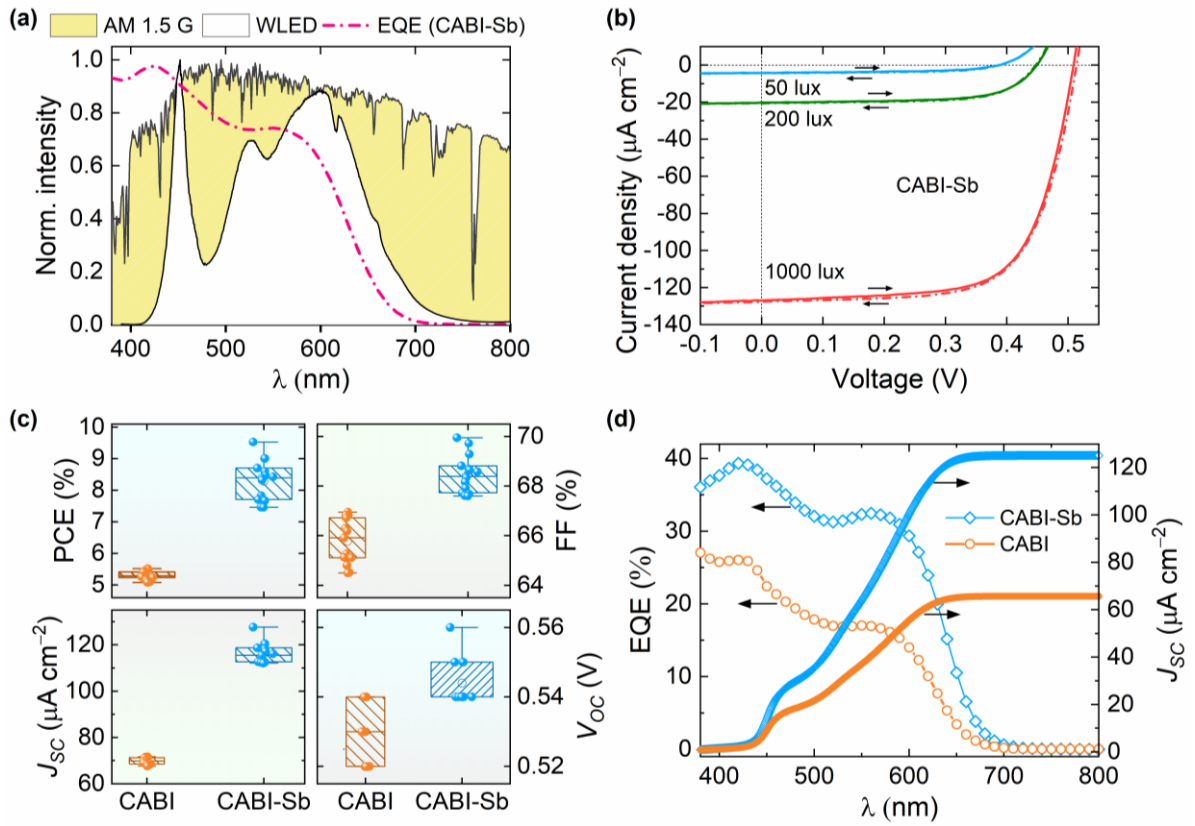

Figure 6. (a) Comparison between the EQE profile of CABI-Sb photovoltaic device, AM 1.5 G (1-Sun) and WLED spectra. b) *J–V* curves (reverse and forward bias scans) of the CABI-Sb device under WLED illumination with various intensities (50, 200, and 1000 lux). c) Statistical distribution of the photovoltaic parameters of the CABI and CABI-Sb IPV devices under 1000 lux WLED illumination. (d) EQE spectra of the devices and their integrated J_{SC}^{EQE} curves over the 4000 K WLED (1000 lux).

The negligible discrepancy[46] of 8% and 3% between the J_{SC} from *J–V* scans and integrated J_{SC} from EQE for CABI (J_{SC}^{J-V} = 72 μA cm^{-2}, J_{SC}^{EQE} = 66 μA cm^{-2}) and CABI-Sb (J_{SC}^{J-V} = 128 μA cm^{-2}, J_{SC}^{EQE} = 125 μA cm^{-2}), respectively (see **Figure 6d**), unequivocally validates our IPV measurements. In order to understand the decrease in V_{OC} (from 0.64 V to 0.51 V) of the champion CABI-Sb device upon reduction of the illumination intensity (from 1-Sun to 1000 lux WLED illumination), we estimate the V_{OC} change (ΔV_{OC}) under zero trap-assisted recombination using the following relation:[47]

$$\Delta V_{OC} = \frac{n_{ID} k_B T}{q} \ln \frac{I_{1-Sun}}{I_{WLED}}$$

where n_{ID}, k_B, T, and q are diode ideality factor (= 1 in the case of only radiative recombination), Boltzmann constant (=1.38×10^{-23} J K^{-1}), temperature (=298 K), and electron charge (=1.6×10^{-}

[19] J), respectively. $I_{1\text{-}Sun}$ (100 mW cm^{-2}) and I_{WLED} (0.0023 mW cm^{-2}, 0.092 mW cm^{-2} and 0.46 mW cm^{-2} at 50 lux, 200 lux and 1000 lux, respectively) are the 1-Sun and WLED illumination intensities, respectively. The resultant ΔV_{OC} values (or, in other words, the V_{OC} losses) are 0.215, 0.18, and 0.14 V at 50, 200, and 1000 lux, respectively. These values closely match the corresponding experimental values of 0.26 (50 lux), 0.20 (200 lux), and 0.13 V (1000 lux) in comparison to the inevitable V_{OC} loss of ≈0.20 V observed in highly efficient IPV devices under low light intensity.[47,48] Although the V_{OC} losses of the CABI-Sb device are low with decreasing illumination intensity, its V_{OC} values still remain low under both 1-Sun and WLED illuminations, similar to the case of CABI-based photovoltaic devices.[8,17,18] Despite the enhancement of the J_{SC} of the devices by Sb alloying by reducing defect formation and carrier self-trapping, the V_{OC} values of the CABI-Sb devices are far from their theoretical limit of ~1.4 eV.[19] This suggests that additional carrier loss mechanisms still exist and need to be identified and addressed to further improve the PCE(i) of the CABI-Sb devices. On the other hand, the FFs of the champion CABI and CABI-Sb devices are ~3% higher under WLED than 1-Sun illuminations. Furthermore, CABI-Sb device exhibits a relatively stable FF trend compared to the pristine CABI device at very low WLED intensities (**Figure 7a**). While CABI device experiences only a moderately larger loss (7%) in the FF than the CABI-Sb counterpart (1.4%) when the WLED intensity decreases up to 200 lux, at even lower light intensities its FF drops abruptly with only a 63% of its initial value retained at 50 lux (see the inset of the **Figure 7a**). On the other hand, the FF of the CABI-Sb device maintains 90% of the original value at the same light intensity of 50 lux. This extremely stable FF trend of CABI-Sb devices with respect to state-of-the-art pnictohalide-based IPVs (CABI,[8,9] $Cs_3Sb_2I_{9-x}Cl_x$[5], or CsMAFA-Sb[10]) can be partly attributed to their higher shunt resistance. In addition, as the number of photogenerated carriers is strongly reduced at the very low light intensity of 50 lux while the trap density does not change with the illumination intensity, large FF losses (as well as V_{OC} losses) are inevitable at very low intensities unless the trap density is minimal. Hence, the FF trend for CABI-Sb devices suggests a reduced defect density in CABI-Sb absorber with respect to pristine CABI, as highlighted by the results of our DFT study and as will be experimentally verified in the following sections. The stable FF and V_{OC} trends result in an impressive PCE(i) of 6.65% for CABI-Sb device at 200 lux, which is much higher than in the case of pristine CABI (PCE(i) = 4.64% at 200 lux).[9] More strikingly, the device delivers a PCE(i) of ~4.26% (with a V_{OC} of 0.38 V) even at 50 lux, i.e., the illuminance range at a typical position (e.g., walls) of IoT sensors in the buildings.[49] It is worth noting that, while CABI-Sb device retains ~45% (9.53%

→ 4.26%) of its initial (at 1000 lux) PCE(i) at 50 lux, CABI reference device delivers only ~18% (5.52% → 1.01%) of the initial PCE(i) at the same light intensity (see **Table 3**).

Table 3. The PCE(i) values of the champion CABI and CABI-Sb devices under varying white light emitting diode (WLED) (4000 K) illumination intensities.

Light intensity	*J-V* scan direction	PCE(i) %	PCE(i) %
		CABI	**CABI-Sb**
1000 lux	Reverse	5.52	9.53
	Forward	5.51	9.45
800 lux	Reverse	5.07	8.03
	Forward	4.99	8.03
600 lux	Reverse	4.82	7.76
	Forward	4.77	7.80
400 lux	Reverse	4.33	7.08
	Forward	4.32	7.02
200 lux	Reverse	3.73	6.65
	Forward	3.71	6.47
100 lux	Reverse	2.81	6.05
	Forward	2.72	5.78
50 lux	Reverse	1.01	4.26
	Forward	0.82	3.85

Carrier dynamics within the bulk and at the interfaces

We examined the light-intensity dependence of V_{OC} of the two types of devices (CABI- and CABI-Sb-based) for understanding the reduced trap-assisted recombination process in CABI-Sb.[5,9] To this aim, we referred to the diode equation, $V_{OC} \approx n_{ID} \left[\frac{k_B T}{q}\right] ln(I)$, where n_{ID} is the ideality factor of the diode, k_B is the Boltzmann constant, and T and q are the temperature and the elementary charge, respectively, and extracted the n_{ID} values for both devices from their V_{OC} vs. WLED intensity (I = 50–1000 lux) semi-log plots. While n_{ID} = 1, in general, specifies the bimolecular (radiative) recombination as the exclusive pathway, n_{ID} > 1 indicates a dominant Shockley-Read-Hall (SRH)-type trap-assisted recombination.[50] The CABI-Sb device shows a lower n_{ID} value (1.62) than that of pristine CABI counterpart (n_{ID} = 1.85), as shown in

Figure 7b. This confirms that the Sb alloying in the CABI devices suppresses the non-radiative, trap-assisted recombination pathways, which may warrant an improved device performance through efficient charge transport and collection.[25] This behavior of CABI-Sb devices agrees with their lower E_U values along with superior J_{SC} and EQE values compared to the case of pristine CABI devices. Furthermore, the exponential factor (α) from the power law dependence of J_{SC} on the WLED light intensity (I) (i.e., $J_{SC} \propto I^{\alpha}$) under short-circuit conditions deals with the extent of defect-assisted recombination and the ability of the electrodes of the photovoltaic device to extract the photogenerated charge carriers.[5,25] The value of $\alpha \approx 1$ (extracted from the log-log plot of J_{SC} vs. *I*, with the light intensity lower limit being 50 lux, see **Figure 7c**) for CABI-Sb device suggests minimized non-geminate recombination losses that contribute to the enhanced J_{SC} values of the device under both 1-Sun and low-intensity WLED illuminations.

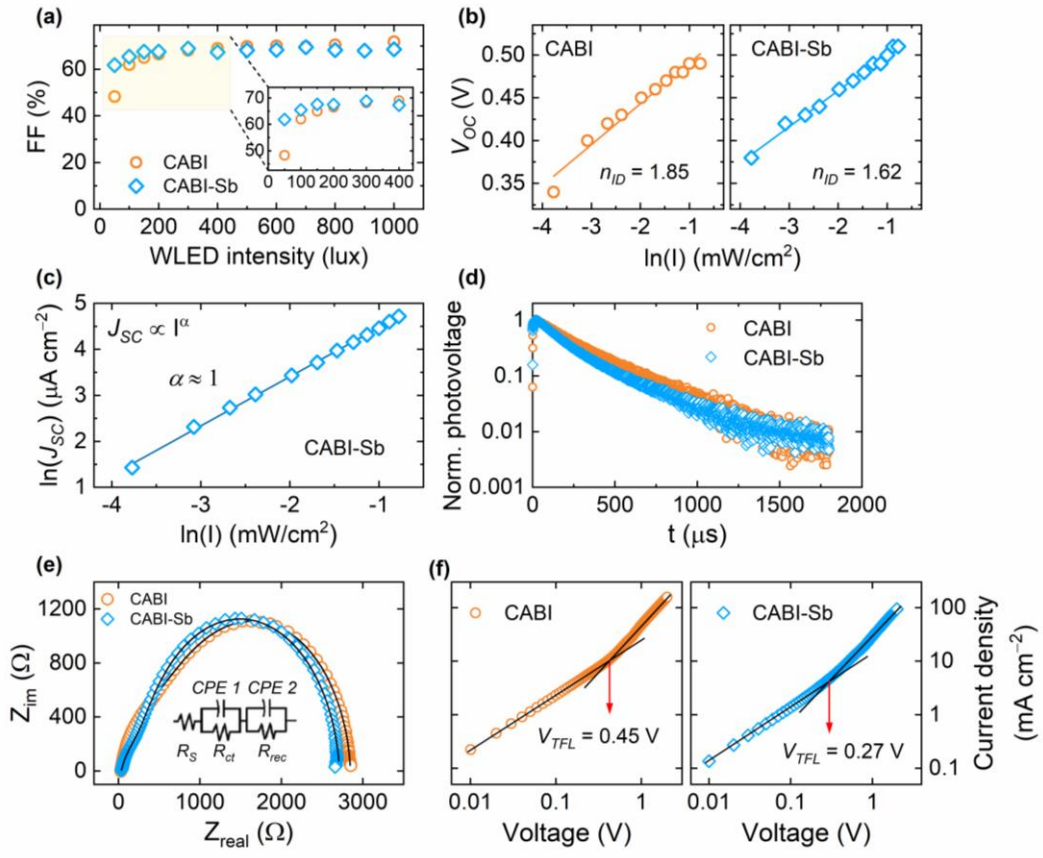

Figure 7. a) Variation of FF of CABI and CABI-Sb devices versus WLED light intensity. The inset shows the FF trend in the 0–450 lux range. b) A semi-log trend of V_{OC} of the CABI-Sb device versus WLED light intensity. c) Log–log plot of J_{SC} trend of the CABI-Sb device versus WLED light intensity. d) Transient photovoltage (TPV) decays of CABI and CABI-Sb devices, excited at 450 nm. e) Nyquist plots recorded at 0.5 V with symbols and lines showing experimental data and the corresponding fits based on the equivalent circuit model,

respectively. f) Dark *J–V* curves (on a log–log scale) of the hole-only devices (ITO/PEDOT:PSS/CABI or CABI-Sb/Spiro-OMeTAD/MoO_3/Au) with the V_{TFL} (trap-filled limit voltage) kink points.

To further understand the superior performance of CABI-Sb IPVs, we investigated the charge carrier dynamics in CABI and CABI-Sb devices by transient photovoltage (TPV) technique. This involves the ultrashort pulse laser excitation of the devices under open circuit conditions to probe into the rate of recombination of the photogenerated charge carriers.[51] Further, the TPV decays provide insights on the kinetics of the accumulated charge carriers at the interfaces between CABI-Sb (or CABI) and ETL or HTL, i.e., the capacitive discharging time, rather than just the bulk carrier lifetimes within the photoactive layer.[51,52] Two comparable decay constants were extracted from the TPV decay curves (**Figure 7d**) of CABI (t_1 = 184 µs and t_2 = 392 µs) and CABI-Sb (t_1 = 148 µs and t_2 = 440 µs) devices (see **Table S7**). The fast decay components (t_1) in CABI and CABI-Sb can be ascribed to the charge carrier recombination assisted by trap states (SRH type) within the bulk and/or at the charge transport layer interface. On the other hand, the slow decay components (t_2) are related to the recombination of long-lived charge carriers. The slow decay represents the slow-back transfer and then recombination of some of the charge carriers trapped at the CABI | charge transport layer interface (i.e., surface defect states) or at the grain/domain boundaries.[51] While the TPV decay of the CABI-Sb device is dominated by the fast component by 79%, the ratios of the amplitudes of slow and fast decay channels are comparable (i.e., A_1:A_2 = 53:47) in the case of the CABI device (**Table S7**). This, in turn, suggests a higher number of deep-level traps in CABI than CABI-Sb, which is in line with the relatively easy formation of iodine vacancies in the case of CABI, as revealed by our first-principles calculations. In summary, the TPV decay data suggests a significant reduction in the undesirable trap-assisted recombination in the CABI-Sb films, attributed to fewer defects within the domains or at their surface arising from their enhanced microstructure. The open-circuit voltage decay (OCVD) for CABI-Sb device monitored under 1000 lux WLED illumination is two times slower than in the case of CABI (**Figure S16a**), suggesting the slower photogenerated recombination time in agreement with the TPV outcomes. The variation of the electron lifetime (τ_n) as a function of the voltage can be estimated from the OCVD curves with the help of the model proposed by Bisquert and co-workers,[53] i.e., $\tau_n = -\frac{k_B T}{e}\left(\frac{dV_{OC}}{dt}\right)^{-1}$, where k_B is the Boltzmann constant, T is the temperature (K), e is the elementary charge, and t is the time after turning off the illumination source. The electron lifetime values of CABI-Sb

device remain higher in the V_{OC} range in comparison with that of CABI device (**Figure S16b**), owing to the reduced recombination at the interface between CABI-Sb and TiO_2,[10,54] thereby supporting the lower trap density upon co-alloying with Sb.

To further probe into the influence of Sb-alloying on charge transfer in CABI devices, electrochemical impedance spectroscopy (EIS) measurements were carried out on CABI-Sb and the pristine CABI cells. The Nyquist plots of the devices are given in **Figure 7e** (the inset shows the equivalent electronic circuit model used to fit the experimental data). The impedance spectra of both CABI and CABI-Sb devices comprise a small arc at the high-frequency region and a bigger semicircle at the low-frequency region. The equivalent circuit model consists of two R(CPE) (where R = resistance and CPE = constant phase element) connected in series. In this model, R_S is the series resistance, R_{ct} and CPE1 are associated with the high frequency charge transfer resistance and capacitance due to non-optimal interfaces,[55] and R_{rec} and CPE2 represent the low frequency recombination resistance and capacitance in the bulk CABI and CABI-Sb layers.[55,56] Since R_{ct} at the high-frequency region is attributed to the extraction of the charge carriers, the R_{ct} of 300 Ω (**Table S8**) of the CABI-Sb device indicates a superior charge extraction compared to the pristine CABI device (R_{ct} = 650 Ω).[55] This is in line with the enhanced J_{SC} of the CABI-Sb devices under 1-Sun and low light intensity (WLED) illuminations. The second semicircle in the low frequency region is dominated by the charge recombination resistance (R_{rec}),[56,57] which is higher for the CABI-Sb device (2377 Ω) compared to the CABI device (2167 Ω). This indicates a significant reduction in charge carrier recombination in the CABI-Sb devices, consistent with the reduced defect density in CABI-Sb than CABI, as supported by DFT-based defect formation energy calculations.

Trap density

The light-intensity dependence trends of the photovoltaic parameters, together with the TPV and EIS analyses, indicate lower trap-assisted recombination in CABI-Sb films with respect to pristine CABI, which is the key to maximizing the V_{OC}, FF, and J_{SC}, particularly at very low-light intensities. This may also imply a reduced trap state density (N_{trap}) in CABI-Sb films, as predicted by our theoretical study. To experimentally corroborate this, the SCLC measurements were performed on hole-only devices with 'ITO/PEDOT:PSS/CABI (or CABI-Sb)/Spiro-OMeTAD/MoO_3/Au' structure. The trap-filled limit voltage (V_{TFL}), i.e., the bias onset at which the current sharply increases, corresponding to the trap-filling region of the dark *J–V* curves, is an indicator of trap densities in the films. The V_{TFL} of 0.27 V for CABI-Sb device is lower

than for CABI device with V_{TFL} = 0.45 V (see **Figure 7f**). The corresponding trap densities, N_{trap}, of the hole-only devices were quantified using $N_{trap} = \frac{2\varepsilon\varepsilon_0 V_{TFL}}{qL^2}$ where ε is the dielectric constant of CABI or CABI-Sb, ε_0 is the vacuum permittivity, q is the elementary or electron charge, and L is the thickness of CABI (316 nm) and CABI-Sb (326 nm) layers. We estimated the ε values (4.89 and 4.79 for CABI and CABI-Sb, respectively) using the many body perturbation theory in the random phase approximation (the data is presented in **Figure S17)**. The trap density, N_{trap} of CABI-Sb device, corresponding to the V_{TFL} value of 0.27 V, is 1.34 × 10^{15} cm^{-3}, which is nearly half the value of that of the pristine CABI device (N_{trap} = 2.44 × 10^{15} cm^{-3}). This strongly supports our finding that the co-alloying of Bi with Sb in CABI is the key to suppressing the defect density, thereby enhancing the photogenerated carrier transfer and collection.

Conclusions

In conclusion, we demonstrate the first alloying of Sb^{3+} in the octahedral sites of Bi^{3+} in perovskite-inspired CABI semiconductor, which enhances the film morphology and inhibits the defect formation. The reduced octahedral distortion upon Sb incorporation suppresses the carrier self-trapping in CABI-Sb, as proved by TA measurements, leading to the generation of more free carriers and, thus, a superior charge collection efficiency. This, in turn, results in IPVs with an improved J_{SC} (from 72 µA cm^{-2} up to 128 µA cm^{-2}) as well as a record PCE(i) approaching 10% under 1000 lux WLED intensity illumination for the CABI-Sb champion device. These findings bring CABI-based devices a significant step closer to their eventual PCE(i) limit of 50–60%. Our theoretical study demonstrates a remarkably increased energy formation for the intrinsic vacancies in CABI upon Sb alloying, resulting in an overall lower defect density than in pristine CABI. The reduced trap density and related bulk and interface recombination in CABI-Sb devices are experimentally verified through various device characterization approaches, i.e., the dependence of V_{OC} and J_{SC} on the indoor light intensity, TPV, EIS, and SCLC measurements.

Bi-Sb alloying, by reducing the intrinsic defects in CABI, proved to be a key strategy for high-performance IPVs for renewable energy generation and consumption, as defects represent the major bottleneck of the performance of lead-free absorbers (particularly wide bandgap ones) under low light intensity illumination. The PCE(i) improvement demonstrated in this study will certainly encourage more studies on wide bandgap perovskite-inspired materials, by endorsing

a straightforward approach to increase their competitivity as low-toxicity, stable, and high-performing IPV absorbers.

Experimental Procedures

Materials

Bismuth iodide (BiI_3), and copper iodide (CuI), Titanium diisopropoxide bis(acetylacetonate) (TDBA) 75 wt.% in isopropanol, dimethylsulfoxide (DMSO), hydroiodic acid (HI, 57%), chlorobenzene (CB, extra dry, 99.8%), acetonitrile (99.9%), and 4-tert-butyilpyridine (4-tBP), bis(trifluoromethane)sulfonimide lithium salt (Li-TFSI, 99.95%), were purchased from Sigma-Aldrich. Tris[2-(1 H-pyrazol-1-yl)− 4-tert-butylpyridine]cobalt(III)tri[bis-(trifluoromethane) sulfonimide] (FK209 Co(III), > 98%) was purchased from Dyenamo. Dimethylformamide (DMF), silver iodide (AgI), and toluene were purchased from Alfa Aesar. Antimony iodide (SbI_3) was purchased from Fisher. 2,2′,7,7′-Tetrakis(N,N-di-p-methoxy phenylamino)-9,9 spirobifluorene (Spiro-OMeTAD) was purchased from Lumtec. Fluorine-doped tin (IV) oxide (FTO) coated glass substrates of 2 cm × 2 cm were purchased from Yingkou Opv Tech New Energy Technology Co.

Film processing of CABI and CABI-Sb

We first prepared two solutions, namely Solution-I and Solution-II as follows. The Solution-I (for CABI) was prepared by mixing BiI_3 (517.1mg), CuI (238.1mg), and AgI (241.8 mg) in 2 ml DMSO: DMF (3:1) and heated at 150 ^oC for 45 min until it became clear and transparent. The Solution-II (for CABI-Sb) was prepared by mixing SbI_3 (176.3mg), CuI (95.2mg), AgI (96.7mg) in 800µl DMSO: DMF (3:1) and stirred overnight to become clear and transparent. CABI-Sb precursor solutions with varying Bi:Sb molar ratios were obtained by mixing Solution-I and Solution-II in the desired ratios. The CABI and CABI-Sb films were deposited by spin-coating (at 3000 rpm for 1 min). Immediately the films were taken annealed in the air for 50 minutes at 50 °C and then for 4 minutes at 150 °C.

Photovoltaic device fabrication

Pre-etched FTO substrates were sonicated for 15 minutes in each step with aqueous Mucasol solution (2% in water), deionized water, acetone, and 2-propanol and the cleaned FTO substrates were dried using nitrogen gas flow. On the as-prepared FTO substrates, a compact titanium dioxide layer (c-TiO_2) layer (thickness ~50 nm) was deposited by spray pyrolysis at 450°C of titanium di-isopropoxide bis(acetylacetonate) solution (0.38 M) and then sintered (at

450°C for 1 hour) in the air. The mesoporous TiO_2 (mp-TiO_2) layer was deposited by spin-coating (4000 rpm per 10 s) of the 30NRD TiO_2 nanoparticle paste/ethanol (0.3 g/1 mL) solution. The mp-TiO_2-coated substrates were calcinated at 450 °C for 30 min in air and then were immediately transferred into a N_2-flled glove box when they were at slightly above 150 °C. The CABI and CABI-Sb absorber layers were deposited on top of mp-TiO_2 substrates. Doped Spiro-OMeTAD (28 mM in CB) was deposited dynamically by spin-coating 80 μL at 1800 rpm for 30 s.[8] After that, the devices were stored overnight in a dry-air atmosphere. Finally, a 100 nm thick gold electrode was thermally evaporated under vacuum (pressure < 10^{-6} mbar) via a metal shadow mask to obtain an active area of 20 mm^2.

XRD

XRD patterns were collected using the Malvern Panalytical Empyrean multipurpose diffractometer with a Cu K_α X-ray source (λ = 0.15418 nm). The X-ray tube was operated at 45 kV and 40 mA. The films were scanned over 10°–60° with a 0.026° step size and step duration of 2998 s/step. The visualization system for the electronic and structural analysis (VESTA) program[58] was used to draw the crystal structures. Structural information was derived from Rietveld refinement using the GSAS software suite. The phase purity of the as-synthesized samples was estimated via Rietveld refinement of the XRD results with the consideration of full refinement of the crystallographic and instrumental parameters in the GSAS program suite.

SEM

The top view and cross-sectional SEM images of the films and devices were collected using a field emission scanning electron microscope (FE-SEM, Zeiss ULTRA plus, Carl Zeiss, Germany) operated at 3kV. EDS spectroscopy (Oxford Instruments X-MaxN 80 EDS) in combination with Zeiss UltraPlus FE-SEM revealed the elemental composition of the films.

XPS

The XPS measurements were performed in ultra-high vacuum employing an Al Kα X-ray source ($h\nu$ = 1486.7 eV) and Argus electron spectrometer (Omicron Nanotechnology GmbH). For the measurement perovskite film samples were spin-coated on FTO glass substrates. The chemical states of elements were determined from the XPS spectra by least-squares fitting of synthetic Gaussian–Lorentzian line shapes after background subtraction. The analysis was made in CasaXPS software version 2.3.25PR1.0.[59] Due to peak overlap, Cu 2p and Sb 3d were analyzed from Cu $2p_{1/2}$ and Sb $3d_{3/2}$ peaks instead of more intensive Cu $2p_{3/2}$ and Sb $3d_{5/2}$. The

second doublet peak was fitted using constrained peak area ratio (2:1 for $p_{3/2}$:$p_{1/2}$ and 3:2 for $d_{5/2}$:$d_{3/2}$) and peak separation (19.8 eV for Cu 2p and 9.34 eV for Sb 3d). The binding energy scale was calibrated according to C 1s (C–C/H) set to 284.8 eV.

Spectroscopic methods

UV-Visible absorption spectra of the CABI and CABI-Sb films were collected on a Shimadzu UV-1800 absorption spectrometer (dual-beam grating), Shimadzu Corporation, Japan. FLS1000 spectrofluorometer (Edinburgh Instruments, UK) was employed to measure steady-state PL spectra of the films. Time-correlated single photon counting (TCSPC) measurements for the TRPL decay were performed on a device equipped with a Picoharp 300 controller and a PDL 800-B driver used for excitation. A Hamamatsu R3809U-50 microchannel plate photomultiplier helped in the detection in 90° configuration.

Ultrafast TA measurements

A Libra F laser system (Coherent Inc.) produced 800 nm light pulses at a repetition rate of 1 kHz, which was decreased to half by a chopper for the sample pumping. The pulse duration (time-resolution) was ≈100 fs, and the measurement system (ExciPro, CDP Inc.) comprised of a silicon CCD array for measurements in the range of visible light. The pump wavelength was tuned by a Topas C optical parametric amplifier (Light Conversion Ltd.), and the white light continuum for the probe pulses was triggered by a water-filled cuvette. The CABI or CABI-Sb film samples were excited at 400 nm with an excitation energy density of 20 μJ cm^{-2}.

***J–V* and EQE measurements**

A Keithley 4250 source-monitor unit (4-wire setup) was used to measure *J–V* curves under simulated solar radiation (100 mW/cm^2 irradiance) illuminated by a class-A++A+A LED-powered solar simulator (SINUS-70 from Wavelabs). Calibration of the device to 1-sun intensity was performed using a Newport 91150-KG5 Reference Cell and Meter. *J–V* curves were obtained under ambient conditions. A quantum efficiency measurement device (QuantX-300, Newport) was used to collect EQE spectra. For the illumination during indoor *J-V* measurements, a WLED (Philips HUE) was used as a light source (color temperature: 4000 K). A PeakTech 5065 digital lux-meter was used to adjust the distance between the light source and solar cell to achieve 50–1000 lux illumination (refer to our previous article for further information about the indoor *J-V* measurements).[9]

TPV and OCVD measurements

The samples were held under 33 mW white light bias obtained from a xenon light source (Oriel Apex fiber illuminator, Newport) directed to the sample through a 1 mm optical fiber and refocused to cover the whole device surface. The output of a Nd:YAG laser (NT342B-AW, Ekspla, ~5 ns pulse width, 10 Hz repetition rate) was directed through an integrated optical parametric oscillator to generate 410 nm excitation pulses spread to ~0.6 cm^2 and filtered with neutral density filters to 63 uW/cm^2 at the sample. The TPV response was monitored with a digitizing oscilloscope (TDS5032B, 1M ohm input impedance, Tektronix Inc.) and extracted by subtracting the bias induced OCV. Powers were measured with Coherent LabMax-TO using PM3 sensor for white light bias and OP-2 VIS sensor for laser pulses.

For the OCVD measurements, the CABI and CABI-Sb photovoltaic devices were illuminated with the WLED (1000 lux) at open-circuit conditions. After the V_{OC} value reached a stable value, the illumination was switched off with a shutter, and the decays of the V_{OC} were collected by means of a potentiostat (Ivium Technologies B.V., Compact Stat).

EIS measurements

The potentiostat (Ivium Technologies B.V., Compact Stat) was used to measure the EIS of the devices. Impedance spectra were collected over the frequency range of 2MHz to 1Hz with an applied voltage of 0.5V in dark conditions. The obtained EIS data were fitted using EIS spectrum analyser software based on the equivalent circuit model.

Trap Density Measurements

Hole-only devices with the structure of ITO/PEDOT:PSS/CABI or CABI-Sb/Spiro-OMe-TAD/MoO_3 (6 nm)/Au (80 nm) were fabricated and the dark *J–V* curves were recorded using Keithley 4250 source-monitor unit and then were used to calculate the trap density. A 150 μL of the PEDOT:PSS (1:1 in DMF) solution was spin-coated onto etched 2 × 2 cm ITO substrates dynamically at 3000 rpm for 40 s.

Computational details

DFT calculations[60] with periodic boundary conditions (PBC) were performed using basis set of numerical atom-centered orbitals (NAO),[61] as implemented in the Fritz Haber Institute ab initio molecular simulations (FHI-aims) code.[62] Within the FHI-aims framework, electrons were described by the zero-order regular approximation (atomic ZORA). A threshold of 1 × 10−6 eV was employed for self-consistency convergence of the total energy. The Perdew–

Burke–Ernzerhof, PBE[63] exchange correlation functional was employed for all geometry optimizations including the Tkatchenko–Scheffler (TS) correction[64,65] accounting for van der Waals dispersion forces. Structures were relaxed until maximum forces acting on each atom were below 0.02 eV $Å^{-1}$. A 4x4x2 and 2x2x2 k-points sampling mesh were used for CABI and CABI-Sb respectively; these values ensure converged energies within 3 meV/f.u. The light-tier1 basis of NAO was used for structural relaxations. The mixed occupancy of Bi/Ag/Sb/Vacancy was simulated via the special quasi-random structure (SQS) approach as implemented in the Alloy Theoretic Automated Toolkit code.[66,67] Electronic calculations have been refined by means of the HSE06 hybrid functional to calculate the projected density of states (pDOS) and the formation energies. The tight-tier1 basis set of NAO was used for refinement.

Author contributions

B. Al-Anesi: Investigation, data curation, formal analysis, validation, visualization, methodology, writing-review & editing. G. K. Grandhi: Conceptualization, investigation, data curation, formal analysis, validation, visualization, methodology, funding acquisition, writing-original draft. A. Pecoraro: Investigation, data curation, formal analysis, validation, visualization, writing-review & editing. V. Sugathan: Investigation, data curation, formal analysis, validation, visualization, writing-review & editing. N.S.M. Viswanath: Investigation, data curation, formal analysis, software, validation, visualization, writing-review & editing. H. Ali-Löytty: Investigation, data curation, formal analysis, validation, visualization, writing-review & editing. M. Liu: Investigation, data curation, formal analysis, visualization, funding acquisition, writing-review & editing. T.-P. Ruoko: Investigation, data curation, formal analysis, validation, visualization, funding acquisition, writing-review & editing. K. Lahtonen: Investigation, data curation, formal analysis, visualization, writing-review & editing. D. Manna: Investigation, data curation, formal analysis, visualization, writing-review & editing. S. Toikkonen: Investigation, data curation, formal analysis. A.B. Muñoz-García: Formal analysis, methodology, software, project administration, resources, supervision, validation, writing-review & editing. M. Pavone: Formal analysis, methodology, software, project administration, resources, supervision, validation, writing-review & editing. P. Vivo: Conceptualization; formal analysis, funding acquisition, project administration, resources, supervision, validation, visualization, writing-original draft.

Conflict of Interest

The authors declare no conflict of interest.

Acknowledgements

P.V. acknowledges the financial support of Jane and Aatos Erkko foundation within the SOL-TECH project. P.V. acknowledges the financial support of Academy of Finland, Decision No. 347772. M.L. thanks the Finnish Cultural Foundation (No. 00220107) for funding. This work is part of the Academy of Finland Flagship Programme, Photonics Research and Innovation (PREIN), Decision No. 320165. This work made use of Tampere Microscopy Center facilities at Tampere University.

References

1 I. Mathews, S. N. Kantareddy, T. Buonassisi and I. M. Peters, *Joule*, 2019, **3**, 1415–1426.

2 M. Yavari, F. Ebadi, S. Meloni, Z. S. Wang, T. C.-J. Yang, S. Sun, H. Schwartz, Z. Wang, B. Niesen and J. Durantini, *J. Mater. Chem. A*, 2019, **7**, 23838–23853.

3 W. Ke, C. C. Stoumpos and M. G. Kanatzidis, *Adv. Mater.*, 2019, **31**, 1803230.

4 J. Cao and F. Yan, *Energy Environ. Sci*, 2021, **14**, 1286.

5 Y. Peng, T. N. Huq, J. Mei, L. Portilla, R. A. Jagt, L. G. Occhipinti, J. L. MacManus-Driscoll, R. L. Z. Hoye and V. Pecunia, *Adv. Energy Mater.*, 2021, **11**, 2002761.

6 K. Rühle and M. Kasemann, in *2013 IEEE 39th Photovoltaic Specialists Conference (PVSC)*, IEEE, 2013, 2651–2654.

7 I. Turkevych, S. Kazaoui, N. Shirakawa and N. Fukuda, *Jpn. J. Appl. Phys.*, 2021, **60**, SCCE06.

8 G. K. Grandhi, B. Al-Anesi, H. Pasanen, H. Ali-Löytty, K. Lahtonen, S. Granroth, N. Christian, A. Matuhina, M. Liu, A. Berdin, V. Pecunia and P. Vivo, *Small*, 2022, **18**, 2203768.

9 G. K. Grandhi, S. Toikkonen, B. Al-Anesi, V. Pecunia and P. Vivo, *Sustain. Energy Fuels*, 2023, **7**, 66.

10 N. Lamminen, G. K. Grandhi, F. Fasulo, A. Hiltunen, H. Pasanen, M. Liu, B. Al-Anesi, A. Efimov, H. Ali-Löytty and K. Lahtonen, *Adv. Energy Mater.*, 2022, 2203175.

11 G. Apostolou, A. Reinders and M. Verwaal, *Energy Sci. Eng.*, 2016, **4**, 69–85.

12 A. S. Teran, J. Wong, W. Lim, G. Kim, Y. Lee, D. Blaauw and J. D. Phillips, *IEEE Trans. Electron Devices*, 2015, **62**, 2170–2175.

13 A. M. Ganose, D. O. Scanlon, A. Walsh and R. L. Z. Hoye, *Nat. Commun.*, 2022, **13**, 1–4.

14 S. R. Rondiya, R. A. Jagt, J. L. MacManus-Driscoll, A. Walsh and R. L. Z. Hoye, *Appl. Phys. Lett.*, 2021, **119**, 220501.

15 H. C. Sansom, G. Longo, A. D. Wright, L. R. V Buizza, S. Mahesh, B. Wenger, M. Zanella, M. Abdi-Jalebi, M. J. Pitcher and M. S. Dyer, *J. Am. Chem. Soc.*, 2021, **143**, 3983–3992.

16 L. R. V. Buizza, A. D. Wright, G. Longo, H. C. Sansom, C. Q. Xia, M. J. Rosseinsky, M. B. Johnston, H. J. Snaith and L. M. Herz, *ACS Energy Lett.*, 2021, **6**, 1729–1739.

17 N. Pai, M. Chatti, S. O. Fürer, A. D. Scully, S. R. Raga, N. Rai, B. Tan, A. S. R. Chesman, Z. Xu, K. J. Rietwyk, S. S. Reddy, Y. Hora, G. A. Sepalage, N. Glück, M. Lira-Cantú, U. Bach and A. N. Simonov, *Adv. Energy Mater.*, 2022, **12**, 2201482.

18 F. Zhang, Z. Hu, B. Zhang, Z. Lin, J. Zhang, J. Chang and Y. Hao, *ACS Appl. Mater. Interfaces*, 2022, **14**, 18498−18505.

19 J. K. W. Ho, H. Yin and S. K. So, *J. Mater. Chem. A*, 2020, **8**, 1717–1723.

20 H. Zhu, A. Erbing, H. Wu, G. J. Man, S. Mukherjee, C. Kamal, M. B. Johansson, H. Rensmo, M. Odelius and E. M. J. Johansson, *ACS Appl. Energy Mater.*, 2020, **3**, 7372–7382.

21 J. Kang, S. Chen, M. Hao, J. Liu, M. Al-Mamun, P. Liu, Y. Wang, H. Yin and H. Zhao, *J. Mater. Chem. A.*, 2022, **10**, 19618−19625.

22 Z. Li, S. R. Kavanagh, M. Napari, R. G. Palgrave, M. Abdi-Jalebi, Z. Andaji-Garmaroudi, D. W. Davies, M. Laitinen, J. Julin and M. A. Isaacs, *J. Mater. Chem. A*, 2020, **8**, 21780–21788.

23 B. Ghosh, B. Wu, X. Guo, P. C. Harikesh, R. A. John, T. Baikie, A. T. S. Wee, C. Guet, T. C. Sum and S. Mhaisalkar, *Adv. Energy Mater.*, 2018, **8**, 1802051.

24 X. Jia and L. Ding, *Sci. China Mater.*, 2019, **62**, 54–58.

25 E. Moustafa, M. Méndez, J. G. Sánchez, J. Pallarès, E. Palomares and L. F. Marsal, *Adv. Energy Mater.*, 2022, 2203241.

26 F. Iyoda, R. Nishikubo, A. Wakamiya and A. Saeki, *ACS Appl. Energy Mater.*, 2020, **3**, 8224–8232.

27 H. C. Sansom, L. R. V Buizza, M. Zanella, J. T. Gibbon, M. J. Pitcher, M. S. Dyer, T. D. Manning, V. R. Dhanak, L. M. Herz and H. J. Snaith, *Inorg. Chem.*, 2021, **60**, 18154–18167.

28 F. Garbassi, *Surf. Interface Anal.*, 1980, **2**, 165–169.

29 K. Du, Q. Tu, X. Zhang, Q. Han, J. Liu, S. Zauscher and D. B. Mitzi, *Inorg. Chem.*, 2017, **56**, 9291–9302.

30 S. Tan, I. Yavuz, N. De Marco, T. Huang, S. Lee, C. S. Choi, M. Wang, S. Nuryyeva, R. Wang and Y. Zhao, *Adv. Mater.*, 2020, **32**, 1906995.

31 Y. Chen, S. Tan, N. Li, B. Huang, X. Niu, L. Li, M. Sun, Y. Zhang, X. Zhang and C. Zhu, *Joule*, 2020, **4**, 1961–1976.

32 M. I. Saidaminov, J. Kim, A. Jain, R. Quintero-Bermudez, H. Tan, G. Long, F. Tan, A. Johnston, Y. Zhao, O. Voznyy and E. H. Sargent, *Nat. Energy*, 2018, **3**, 648–654.

33 K. Nishimura, D. Hirotani, G. Kapil, C. H. Ng, K. Hamada, K. Akmal, R. Teresa, S. Qing, T. Minemoto and K. Yoshino, in *Proceedings of International Conference on Hybrid and Organic Photovoltaics (HOPV19)*, 2022.

34 C. Zhu, X. Niu, Y. Fu, N. Li, C. Hu, Y. Chen, X. He, G. Na, P. Liu and H. Zai, *Nat. Commun.*, 2019, **10**, 1–11.

35 M. Liu, S. Kasi Matta, H. Ali-Löytty, A. Matuhina, G. Krishnamurthy Grandhi, K. Lahtonen, S. P. Russo and P. Vivo, *Nano Lett.*, 2021, **22**, 311–318.

36 J. H. Han, T. Samanta, Y. M. Park, H. Bin Cho, J. W. Min, S. J. Hwang, S. W. Jang and W. Bin Im, *Chem. Eng. J.*, 2022, **450**, 138325.

37 B. Yang and K. Han, *J. Phys. Chem. Lett.*, 2021, **12**, 8256–8262.

38 Z. Li, Y.-T. Huang, L. Mohan, S. J. Zelewski, R. H. Friend, J. Briscoe and R. L. Z. Hoye, *Sol. RRL*, 2022, **6**, 2200749.

39 S.-H. Jeong, J. Park, T.-H. Han, F. Zhang, K. Zhu, J. S. Kim, M.-H. Park, M. O. Reese, S. Yoo and T.-W. Lee, *Joule*, 2020, **4**, 1206–1235.

40 S. Hosseini and M. Adelifard, *Phys. status solidi*, 2021, **218**, 2000774.

41 Z. Hawash, L. K. Ono and Y. Qi, *Adv. Mater. Interfaces*, 2016, **3**, 1600117.

42 S. Zeiske, O. J. Sandberg, N. Zarrabi, C. M. Wolff, M. Raoufi, F. Peña-Camargo, E. Gutierrez-Partida, P. Meredith, M. Stolterfoht and A. Armin, *J. Phys. Chem. Lett.*, 2022, **13**, 7280–7285.

43 C. H. Peters, I. T. Sachs-Quintana, W. R. Mateker, T. Heumueller, J. Rivnay, R. Noriega, Z. M. Beiley, E. T. Hoke, A. Salleo and M. D. McGehee, *Adv. Mater.*, 2012, **24**, 663–668.

44 R. Steim, T. Ameri, P. Schilinsky, C. Waldauf, G. Dennler, M. Scharber and C. J. Brabec, *Sol. Energy Mater. Sol. Cells*, 2011, **95**, 3256–3261.

45 D. Glowienka and Y. Galagan, *Adv. Mater.*, 2022, **34**, 2105920.

46 M. Saliba and L. Etgar, *ACS Energy Lett.*, 2020, **5**, 2886–2888.

47 H. Yin, J. K. W. Ho, S. H. Cheung, R. J. Yan, K. L. Chiu, X. Hao and S. K. So, *J. Mater. Chem. A*, 2018, **6**, 8579–8585.

48 Y. Cui, Y. Wang, J. Bergqvist, H. Yao, Y. Xu, B. Gao, C. Yang, S. Zhang, O. Inganäs and F. Gao, *Nat. Energy*, 2019, **4**, 768–775.

49 S. K. Thomas, A. Pockett, K. Seunarine, M. Spence, D. Raptis, S. Meroni, T. Watson, M. Jones and M. J. Carnie, *IoT*, 2022, **3**, 109–121.

50 W. Tress, M. Yavari, K. Domanski, P. Yadav, B. Niesen, J. P. C. Baena, A. Hagfeldt and M. Graetzel, *Energy Environ. Sci.*, 2018, **11**, 151–165.

51 R. Hidayat, A. A. Nurunnizar, A. Fariz, E. S. Rosa, T. Oizumi, A. Fujii and M. Ozaki, *Sci. Rep.*, 2020, **10**, 1–13.

52 D. Kiermasch, A. Baumann, M. Fischer, V. Dyakonov and K. Tvingstedt, *Energy*

Environ. Sci., 2018, **11**, 629–640.

53 A. Zaban, M. Greenshtein and J. Bisquert, *ChemPhysChem*, 2003, **4**, 859–864.

54 F. Di Giacomo, V. Zardetto, G. Lucarelli, L. Cinà, A. Di Carlo, M. Creatore and T. M. Brown, *Nano Energy*, 2016, **30**, 460–469.

55 A. Guerrero, J. Bisquert and G. Garcia-Belmonte, *Chem. Rev.*, 2021, **121**, 14430–14484.

56 Z. Chen, Q. Wang, Y. Xu, R. Zhou, L. Zhang, Y. Huang, L. Hu, M. Lyu and J. Zhu, *ACS Appl. Mater. Interfaces*, 2021, **13**, 24654–24661.

57 Y. Guo, X. Yin, J. Liu and W. Que, *J. Mater. Chem. A*, 2019, **7**, 19008–19016.

58 K. Momma and F. Izumi, *J. Appl. Crystallogr.*, 2011, **44**, 1272–1276.

59 N. Fairley, V. Fernandez, M. Richard-Plouet, C. Guillot-Deudon, J. Walton, E. Smith, D. Flahaut, M. Greiner, M. Biesinger and S. Tougaard, *Appl. Surf. Sci. Adv.*, 2021, **5**, 100112.

60 K. Burke, *J. Chem. Phys.*, 2012, **136**, 150901.

61 V. Blum, R. Gehrke, F. Hanke, P. Havu, V. Havu, X. Ren, K. Reuter and M. Scheffler, *Comput. Phys. Commun.*, 2009, **180**, 2175–2196.

62 V. Havu, V. Blum, P. Havu and M. Scheffler, *J. Comput. Phys.*, 2009, **228**, 8367–8379.

63 J. P. Perdew, K. Burke and M. Ernzerhof, *Phys. Rev. Lett.*, 1996, **77**, 3865.

64 A. Tkatchenko and M. Scheffler, *Phys. Rev. Lett.*, 2009, **102**, 73005.

65 A. Tkatchenko, R. A. DiStasio Jr, R. Car and M. Scheffler, *Phys. Rev. Lett.*, 2012, **108**, 236402.

66 A. Van De Walle, M. Asta and G. Ceder, *Calphad*, 2002, **26**, 539–553.

67 A. van de Walle, R. Sun, Q.-J. Hong and S. Kadkhodaei, *Calphad*, 2017, **58**, 70–81.